RUSC2 and WDR47 oppositely regulate kinesin–1-dependent distribution of ATG9A to the cell periphery

Carlos M. Guardia[a], Akansha Jain[a], Rafael Mattera[a], Alex Friefeld[a], Yan Li[b], and Juan S. Bonifacino[a,*]

[a]Neurosciences and Cellular and Structural Biology Division, Eunice Kennedy Shriver National Institute of Child Health and Human Development, [b]Proteomics Core Facility, National Institute of Neurological Disorders and Stroke, National Institutes of Health, Bethesda, MD 20892

ABSTRACT **Autophagy-related protein 9 (ATG9) is a transmembrane protein component of the autophagy machinery that cycles between the *trans*-Golgi network (TGN) in the perinuclear area and other compartments in the peripheral area of the cell. In mammalian cells, export of the ATG9A isoform from the TGN into ATG9A-containing vesicles is mediated by the adaptor protein 4 (AP-4) complex. However, the mechanisms responsible for the subsequent distribution of these vesicles to the cell periphery are unclear. Herein we show that the AP–4-accessory protein RUSC2 couples ATG9A-containing vesicles to the plus-end-directed microtubule motor kinesin-1 via an interaction between a disordered region of RUSC2 and the kinesin-1 light chain. This interaction is counteracted by the microtubule-associated protein WDR47. These findings uncover a mechanism for the peripheral distribution of ATG9A-containing vesicles involving the function of RUSC2 as a kinesin-1 adaptor and WDR47 as a negative regulator of this function.**

Monitoring Editor
Michael Marks
Children's Hospital of Philadelphia

Received: Jun 7, 2021
Revised: Aug 10, 2021
Accepted: Aug 18, 2021

INTRODUCTION

Intracellular organelles are able to move throughout the cytoplasm, allowing them to distribute their activities to all regions of the cell (van Bergeijk *et al.*, 2016; Bonifacino and Neefjes, 2017). Directed, long-range movement is driven by coupling of the organelles to microtubule motors such as kinesins and dynein-dynactin, which mediate transport toward microtubule plus ends (i.e., anterograde transport) and minus ends (i.e., retrograde transport), respectively. This coupling is often mediated by adaptor proteins that connect the organelles to the motors in a regulated manner. Examples of these mechanisms are those that control the movement of the main organelles involved in autophagy: autophagosomes, and lysosomes (Bento *et al.*, 2016). In mammalian cells, autophagosomes are coupled to kinesin-1 via FYCO1 (Pankiv *et al.*, 2010; Nieto-Torres *et al.*, 2021) and to dynein-dynactin via JIP1 (Fu *et al.*, 2014), JIP3 (Cason *et al.*, 2021), HAP1 (Cason *et al.*, 2021), and/or RILP (Wijdeven *et al.*, 2016; Khobrekar *et al.*, 2020). Lysosomes are also coupled to kinesin-1 via SKIP (Dumont *et al.*, 2010; Rosa-Ferreira and Munro, 2011; Pu *et al.*, 2015; Sanger *et al.*, 2017) and to dynein-dynactin via JIP3/JIP4 (Drerup and Nechiporuk, 2013; Gowrishankar *et al.*, 2017, 2021; Willett *et al.*, 2017) and/or RILP (Jordens *et al.*, 2001). These interactions are often regulated by small GTPases such as RAB7 and ARL8, which recruit the adaptors to the organelles and/or activate them for interaction with the motors (Jordens *et al.*, 2001; Pankiv *et al.*, 2010; Rosa-Ferreira and Munro, 2011; Mrakovic *et al.*, 2012; Keren-Kaplan and Bonifacino, 2021). Additional kinesins, adaptors, and regulators have been implicated in the microtubule-dependent

This article was published online ahead of print in MBoC in Press (http://www.molbiolcell.org/cgi/doi/10.1091/mbc.E21-06-0295) on August 25, 2021.

Author contributions: J.S.B. and C.M.G. conceived the project, designed the experiments, and wrote the manuscript; C.M.G. performed most of the experiments, analyzed the data, and prepared the figures; A.J. conducted the kinesin screen and helped with manuscript preparation; R.M. and A.F. conducted Y2H experiments and contributed to manuscript preparation; Y.L. performed mass spectrometry analysis; all the authors edited the final version of the manuscript.

Competing interest statement: The authors declare no competing interests.

*Address correspondence to: Juan S. Bonifacino (juan.bonifacino@nih.gov).

Abbreviations used: AD, activation domain; BD, binding domain; CC, coiled coil; GFP, green fluorescent protein; HSP, hereditary spastic paraplegia; KD, knockdown; KLC, kinesin light chain; KO, knockout; PAS, preautophagosomal structure; PBS, phosphate-buffered saline; TfR, transferrin receptor; tGFP, TurboGFP; TGN, *trans*-Golgi network; TPR, tetratricopeptide repeat; WDR47, WD40-repeat domain 47; WT, wild type; Y2H, yeast two-hybrid.

transport of both autophagosomes and lysosomes in various organisms, underscoring the complexity of these mechanisms (Santama *et al.*, 1998; Matsushita *et al.*, 2004; Rocha *et al.*, 2009; Pu *et al.*, 2015; Raiborg *et al.*, 2015; Guardia *et al.*, 2016; Mauvezin *et al.*, 2016; Wijdeven *et al.*, 2016; Willett *et al.*, 2017). Interference with components of these machineries reduces the movement of autophagosomes and/or lysosomes, decreasing autophagosome–lysosome fusion and thus impairing autophagy (Ravikumar *et al.*, 2005; Muhammad *et al.*, 2015; Jia *et al.*, 2017; Bejarano *et al.*, 2018; De Pace *et al.*, 2020).

In addition to autophagosomes and lysosomes, other organelles contribute to the process of autophagy, and their motility could potentially influence the efficiency of the process. Unique among these organelles are membrane-bound compartments containing ATG9, a key transmembrane component of the core autophagy machinery (Zavodszky *et al.*, 2013; Noda, 2017). ATG9 proteins are highly conserved in different species and present in all mammalian cells. Whereas in yeast there is a single Atg9 protein (Noda *et al.*, 2000), in mammals there are two ATG9 paralogs: the ubiquitously expressed ATG9A and the tissue-specific ATG9B (predominantly expressed in placenta and neuroendocrine cells) (Yamada *et al.*, 2005). Recent cryo-EM analyses of yeast and human ATG9A showed that the protein assembles into a homotrimer, with each protomer comprising four transmembrane α-helices, and N- and C-terminal domains facing the cytosol (Guardia *et al.*, 2020; Maeda *et al.*, 2020; Matoba *et al.*, 2020). Furthermore, biochemical analyses revealed that ATG9 proteins function as scramblases that translocate phospholipids between the two membrane bilayers (Maeda *et al.*, 2020; Matoba *et al.*, 2020; Ghanbarpour *et al.*, 2021), thus contributing to the expansion of the autophagosomal membrane (Hayashi-Nishino *et al.*, 2009; Ylä-Anttila *et al.*, 2009; Mari *et al.*, 2010; Yamamoto *et al.*, 2012; Graef *et al.*, 2013; Suzuki *et al.*, 2013; Nishimura *et al.*, 2017; Gómez-Sánchez *et al.*, 2018). ATG9 proteins normally cycle between the *trans*-Golgi network (TGN) in the perinuclear area of the cell and preautophagosomal structures (PAS) distributed throughout the cytoplasm, either directly or via intermediate compartments such as a endosomes, the plasma membrane, or other ATG9 reservoirs (Young *et al.*, 2006; Mari *et al.*, 2010; Ohashi and Munro, 2010; Yamamoto *et al.*, 2012; Popovic and Dikic, 2014; Imai *et al.*, 2016; Mattera *et al.*, 2017; Davies *et al.*, 2018). At least some of these transport events are mediated by small (30–60 nm) vesicles referred to as ATG9 vesicles (Yamamoto *et al.*, 2012).

Export of mammalian ATG9A from the TGN was recently shown to depend on recognition of a tyrosine-based sequence (YQRLE) in the cytosolic domain of ATG9A by AP-4 (Mattera *et al.*, 2017), a complex of four subunits named ε, β4, μ4, and σ4 (Dell'Angelica *et al.*, 1999; Hirst *et al.*, 1999). This recognition promotes incorporation of ATG9A into budding AP–4-coated vesicles, which eventually uncoat to generate small vesicles carrying ATG9A. Knockout (KO) or knockdown (KD) of AP-4 subunits in various cell types results in the accumulation of ATG9A at the TGN, with consequent defects in autophagy (Mattera *et al.*, 2017; Davies *et al.*, 2018; De Pace *et al.*, 2018; Ivankovic *et al.*, 2020). Moreover, mutations in genes encoding AP-4 subunits in mice (Matsuda *et al.*, 2008; De Pace *et al.*, 2018; Ivankovic *et al.*, 2020) and humans (Verkerk *et al.*, 2009; Abou Jamra *et al.*, 2011; Behne *et al.*, 2020) cause neurological defects characteristic of complicated hereditary spastic paraplegia (HSP), which may result from reduced export of ATG9A from the TGN and ensuing autophagic defects.

In line with the importance of organelle motility in autophagy, proteomics analyses identified several AP-4 interactors that may couple ATG9A vesicles to microtubule motors. One of these interactors is the FHF complex (Mattera *et al.*, 2020), an assembly of FHIP, HOOK, and FTS subunits (Xu *et al.*, 2008) that was previously shown to function as an activating adaptor for dynein-dynactin (Bielska *et al.*, 2014; Schroeder and Vale, 2016). Silencing of FHF subunits redistributes ATG9A from the central to the peripheral area of the cell (Mattera *et al.*, 2020), consistent with inhibition of dynein–dynactin-driven retrograde transport of ATG9A vesicles. Another AP-4 interactor is a protein known as RUSC2 or iporin (Davies *et al.*, 2018), which comprises a long disordered region followed by a RUN domain, a shorter disordered region and an SH3 domain (Bayer *et al.*, 2005) (Figure 1A). Overexpression of RUSC2 was shown to redistribute ATG9A toward the cell periphery, particularly to cell vertices (also referred to as cell protrusions or tips) (Davies *et al.*, 2018), where microtubule plus ends are most concentrated. However, at present it is unknown if this effect reflects a role for RUSC2 as a kinesin adaptor, a dynein-dynactin inhibitor, or some other kind of regulator. Furthermore, even if RUSC2 were to function as a kinesin adaptor, the identity of the kinesin involved in the peripheral distribution of mammalian ATG9A remains to be established.

To address the function of RUSC2, we performed an siRNA screen of the 29 kinesins expressed in HeLa cells (Maliga *et al.*, 2013) for their potential role in RUSC2-induced redistribution of ATG9A toward the cell periphery. This screen revealed that kinesin-1, a tetramer composed of two kinesin heavy chains (KIF5B in HeLa cells) and two light chains (KLC2 in HeLa cells) (Verhey *et al.*, 2011), is essential for ATG9A redistribution. Furthermore, we found that RUSC2 interacts with kinesin-1 through KLC2, and that the disordered region between the RUN and SH3 domains of RUSC2 is required for both RUSC2-induced peripheral redistribution of ATG9A and interaction with KLC2. Finally, we identified the WD40-repeat-containing protein WDR47/nemitin as an inhibitor of RUSC2-induced, kinesin–1-driven redistribution of ATG9A toward the cell periphery. These results thus uncovered a mechanism for the coupling of ATG9A vesicles to kinesin-1 that enables regulated anterograde transport of these vesicles in mammalian cells.

RESULTS

RUSC2 promotes ATG9A redistribution to the cell periphery

In HeLa cells, endogenous ATG9A normally localizes to a perinuclear structure characteristic of the TGN and to peripheral puncta that may correspond to PAS, endosomes, or related organelles (Figure 1B). As previously reported (Davies *et al.*, 2018), transient transfection with a plasmid encoding full-length RUSC2 (Figure 1A) tagged with monomeric green fluorescent protein (GFP; GFP-RUSC2) caused partial redistribution of endogenous ATG9A to cell vertices (Figure 1B, arrows), albeit in only ~30% of the GFP–RUSC2-expressing cells (Supplemental Figure S1A). In contrast, overexpression of GFP-RUSC2 had no noticeable effect on the distribution of early/recycling endosomes labeled for endogenous transferrin receptor (TfR) or late endosomes/lysosomes labeled for endogenous CD63 (Figure 1C). Stable transduction with a lentiviral vector encoding RUSC2 tagged with dimeric TurboGFP (tGFP) resulted in partial redistribution of ATG9A to cell vertices in ~90% of the cells (Supplemental Figure S1, A and B). In both cases, the tagged RUSC2 constructs colocalized with ATG9A at the cell vertices (Figure 1B; Supplemental Figure S1B, arrows). Quantification of ATG9A distribution by shell analysis confirmed the peripheral redistribution of ATG9A by tagged RUSC2 overexpression (Figure 1, D and E; Supplemental Figure S1C). CRISPR-Cas9 KO of the ε subunit of AP-4 in HeLa cells (Mattera *et al.*, 2017) prevented the tGFP–RUSC2-induced redistribution of ATG9A to cell vertices (Supplemental Figure S1, D and E), confirming that AP-4 is required for RUSC2 to redistribute ATG9A

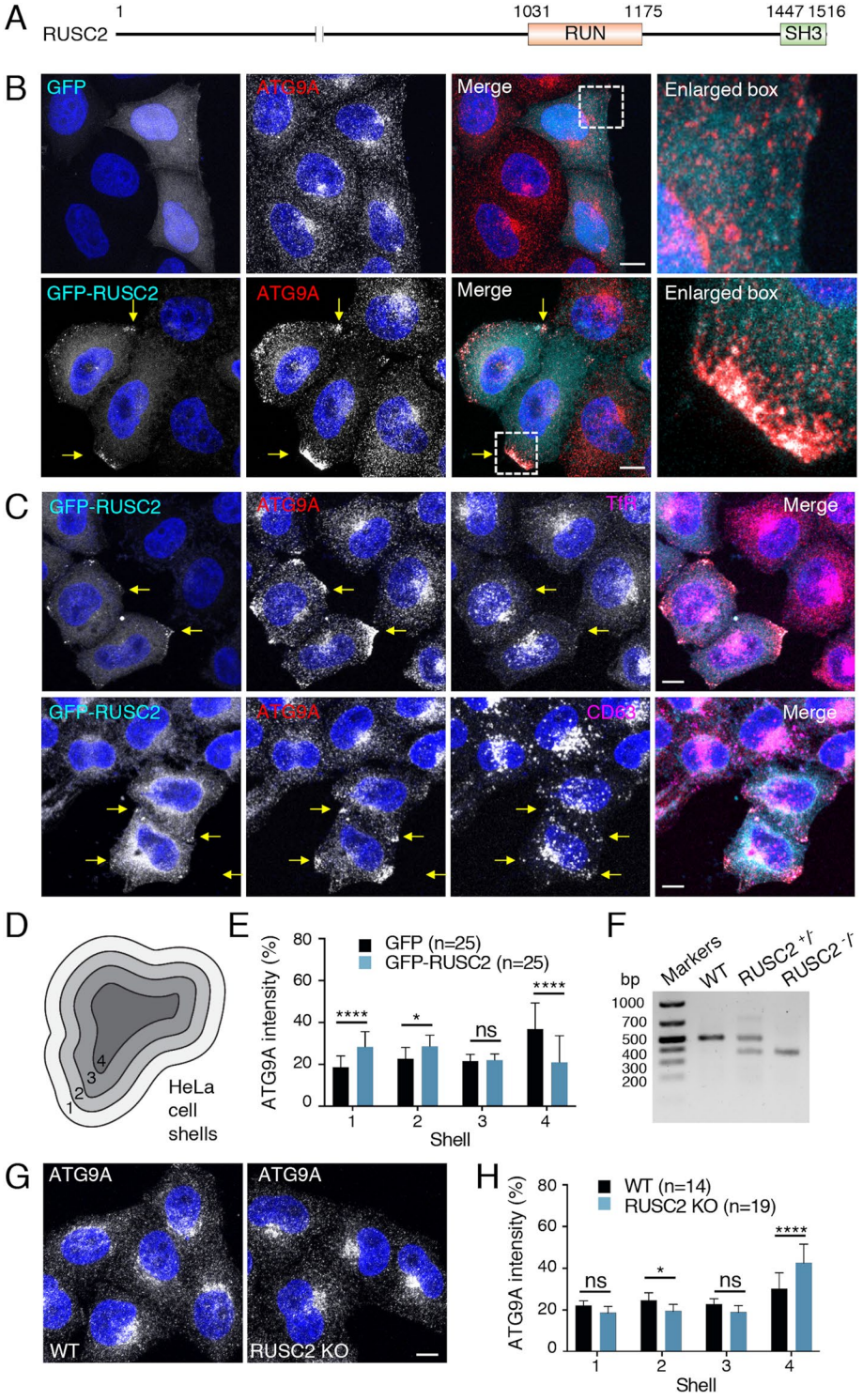

FIGURE 1: RUSC2 controls the cytoplasmic distribution of ATG9A. (A) Schematic representation of full-length human RUSC2 indicating the RUN (1031–1175) and SH3 (1447–1516) domains. (B) HeLa cells were transiently transfected with plasmids encoding GFP or GFP-RUSC2 (cyan), immunostained for endogenous ATG9A (red), and counterstained for nuclei (DAPI) (blue). Cells were imaged by confocal microscopy. Single channels are shown in inverted grayscale with nuclei in blue. Scale bars: 10 µm. Images on the rightmost column are fivefold enlargements of the boxed areas. (C) HeLa cells transiently overexpressing GFP-RUSC2 (cyan) were immunostained for endogenous ATG9A (red) together with TfR or CD63 (magenta), counterstained with DAPI (blue), and imaged by confocal microscopy. Scale bars: 10 µm. Single-channel images are shown in inverted grayscale with DAPI staining in blue. The arrows in panels B and C point to GFP-RUSC2 and ATG9A at vertices of transfected cells. (D) Schematic representation of shell analysis in which the cytoplasm was divided in four regions, with 1 being the most peripheral and 4 being the most central. (E) Quantification of the distribution of ATG9A in GFP- and GFP–RUSC2-overexpressing cells by shell analysis from experiments such as that shown in panel B. Results are expressed as the percentage of the total intensity in each shell region. Values are the mean ± SD from the indicated number of cells (n) in three independent experiments. The statistical significance of the differences was determined using two-way ANOVA followed by Sidak's multiple comparison test. *$p < 0.05$; ****$p < 0.0001$; ns $p > 0.05$, not significant. (F) PCR analysis of genomic DNA from RUSC2+/+ (WT), RUSC2+/– and RUSC2–/– (RUSC2-KO) cells using the primers shown in Supplemental Figure S1F. The positions of DNA size markers are indicated on the left. (G) WT and RUSC2-KO HeLa cells were immunostained for endogenous ATG9A and counterstained for nuclei with DAPI (blue). Cells were imaged by confocal microscopy. Scale bar: 10 µm. (H) Quantification of the distribution of ATG9A in WT and RUSC2-KO cells by shell analysis, as described for panels D and E.

(Davies *et al.*, 2018). Finally, CRISPR-Cas9 KO of the gene encoding RUSC2 (Figure 1F; Supplemental Figure S1F) increased ATG9A localization to the perinuclear area of the cell (Figure 1, G and H). Taken together, these experiments confirmed that RUSC2 specifically promotes AP–4-dependent redistribution of ATG9A toward the peripheral cytoplasm (Davies *et al.*, 2018).

The kinesin-1 heavy chain KIF5B is required for RUSC2-induced redistribution of ATG9A

We hypothesized that RUSC2 promotes redistribution of ATG9A to the cell periphery by coupling ATG9A vesicles to a kinesin molecule, analogously to the role of the adaptor protein SKIP in coupling lysosomes to kinesin-1 (Dumont *et al.*, 2010; Rosa-Ferreira and Munro, 2011; Pu *et al.*, 2015; Guardia *et al.*, 2016; Keren-Kaplan and Bonifacino, 2021). To test this hypothesis, we conducted an siRNA screen in which we individually silenced each of the 29 kinesins expressed in HeLa cells (Maliga *et al.*, 2013) (Figure 2, A and B) and examined the effect of this silencing on ATG9A redistribution induced by GFP-RUSC2 (Figure 2, A–E; Supplemental Figure S2). We observed that only KD of KIF5B, the ubiquitous form of the kinesin-1 heavy chain (Tanaka *et al.*, 1998), prevented the GFP–RUSC2-induced redistribution of ATG9A to cell vertices (Figure 2, B–E; Supplemental Figure S2), whereas KD of KIF1B (Nangaku *et al.*, 1994) (Figure 2, B–E; Supplemental Figure S2) or the other

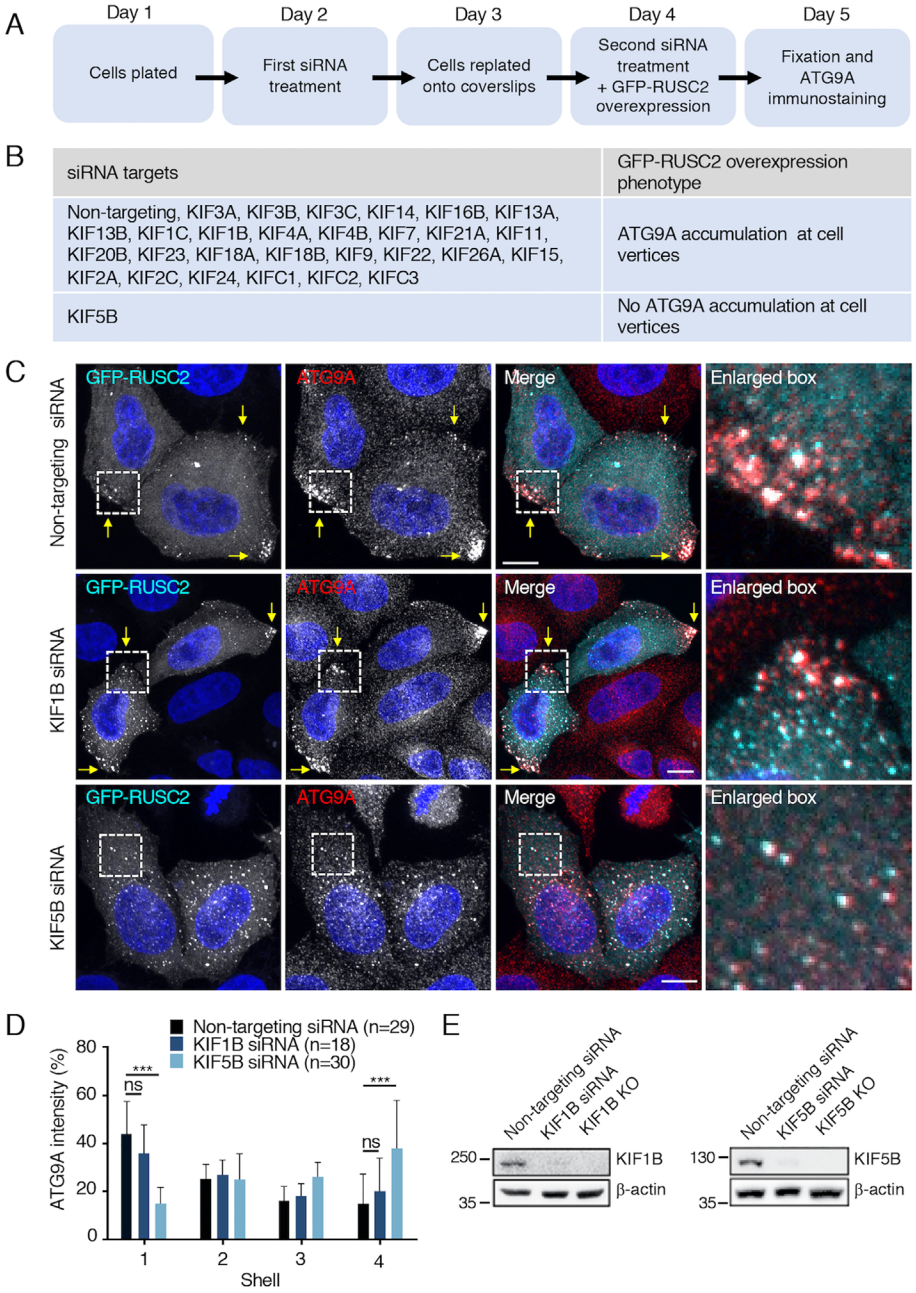

FIGURE 2: KD of KIF5B prevents RUSC2-induced redistribution of ATG9A to cell vertices. (A) Flowchart of siRNA screen. (B) Summary of results from siRNA screen. Representative immunofluorescence microscopy images are shown in panel C and Supplemental Figure S2. (C) HeLa cells treated with nontargeting, KIF1B, or KIF5B siRNAs were transiently transfected with a plasmid encoding GFP-RUSC2 (cyan) according to the protocol in panel A, immunostained for endogenous ATG9A (red), counterstained for nuclei (DAPI) (blue), and examined by confocal microscopy. Scale bars: 10 μm. Single-channel images are shown in inverted grayscale with DAPI staining in blue. Images on the rightmost column are fivefold enlargements of the boxed areas in the merge panels. Arrows point to GFP-RUSC2 and ATG9A at vertices of transfected cells. (D) Quantification of the distribution of ATG9A by shell analysis (see scheme in Figure 1D). Values are the mean ± SD from the number of cells (n) indicated in the figure in three independent experiments. The statistical significance of the differences was determined using two-way ANOVA followed by Sidak's multiple comparison test. ***$p < 0.001$; ns $p > 0.05$, not significant. (E) Immunoblot analysis of whole-cell lysates from WT HeLa cells treated with non-targeting, KIF1B, or KIF5B siRNAs and from KIF1B- or KIF5B-KO HeLa cells. Immunoblots were probed with antibodies to KIF1B, KIF5B, or β-actin (loading control). The positions of molecular mass markers (in kDa) are indicated on the left.

27 kinesins (Figure 2B; Supplemental Figure S2) had no effect. Similarly, CRISPR-Cas9 KO of KIF5B, but not KIF1B (Jia *et al.*, 2017) (Figure 2E), abrogated the ability of GFP-RUSC2 to redistribute ATG9A to cell vertices (Figure 3, A and B). In both KIF5B-KD and KIF5B-KO cells, GFP-RUSC2 localized to cytoplasmic puncta containing ATG9A (Figures 2C and 3A), indicating that RUSC2 associates with ATG9A vesicles independently of KIF5B. From these experiments, we concluded that, at least in HeLa cells, the ability of RUSC2 to distribute ATG9A to the cell periphery is dependent on kinesin-1.

RUSC2 interacts with the kinesin-1 light chain

To determine if the function of RUSC2 is mediated by physical interaction with kinesin-1, we performed coimmunoprecipitation experiments (Figure 4A). In these experiments, we used HeLa cells stably transduced with a lentiviral vector encoding RUSC2 tagged with tGFP because of the higher percentage of expressing cells and the stronger activity of this construct (Supplemental Figure S1, A–C). We observed that tGFP-RUSC2, but not tGFP, coimmunoprecipitated with the endogenous KIF5B and KLC2 chains of kinesin-1 (Figure 4A). We also observed specific coimmunoprecipitation of tGFP-RUSC2 with endogenous ATG9A (Figure 4A).

Next, we used a yeast two-hybrid (Y2H) system to confirm the interaction of RUSC2 with kinesin-1 and to determine if this interaction was direct. To facilitate this analysis, we split the large (1516 amino acid) RUSC2 protein (Figure 1A) into three fragments spanning amino acids 1–365, 366–960, and 961–1516 and expressed the fragments as fusions to the Gal4 transcription activation domain (AD). In addition, we expressed full-length KLC2 and a construct including the coiled-coil (CC) and tail domains of KIF5B (amino acids 326–963) (i.e., "motorless" KIF5B) (Coy *et al.*, 1999; Kimura *et al.*, 2005) fused to the Gal4 DNA-binding domain (BD). As controls, we showed that the tumor suppressor protein p53 did not interact with any of the RUSC2 constructs (negative control) but interacted with the SV40 large T antigen (positive control) (Figure 4B). Using this system, we found that KLC2 specifically interacted with the 961–1516 fragment of RUSC2 comprising the RUN, second disordered, and SH3 domains, whereas the motorless KIF5B did not interact with any part of RUSC2 (Figure 4B).

Further deletion analyses revealed that the minimal region of RUSC2 that interacts with KLC2 spans amino acids 1266–1441

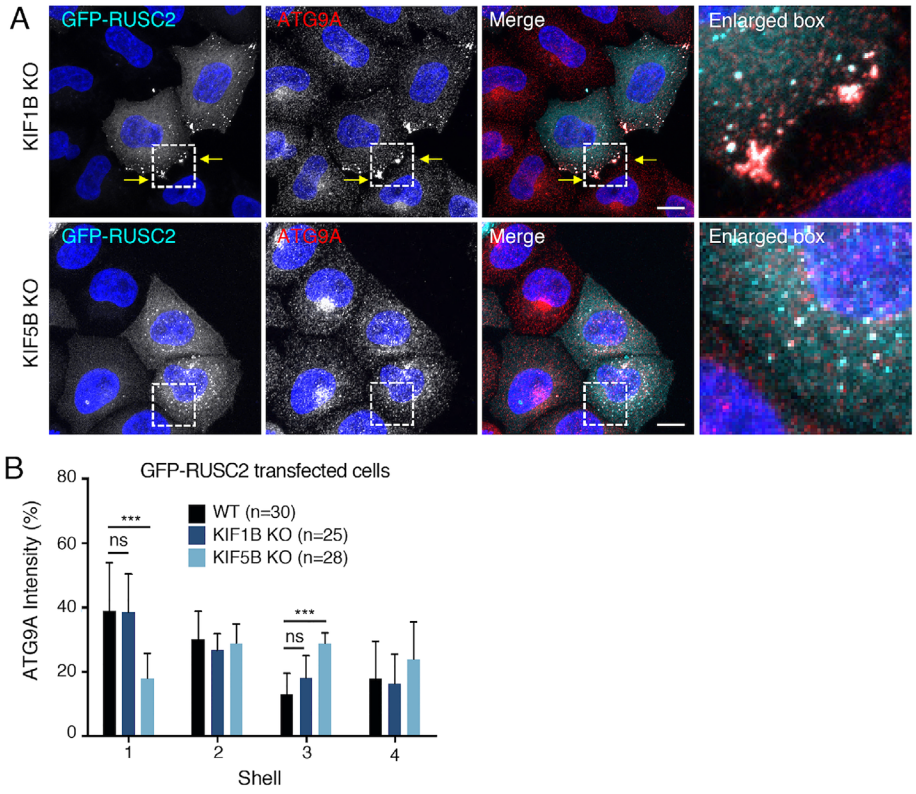

FIGURE 3: KO of KIF5B prevents RUSC2-induced redistribution of ATG9A to cell vertices. (A) KIF1B-KO or KIF5B-KO HeLa cells were transiently transfected with a plasmid encoding GFP-RUSC2 (cyan), immunostained for endogenous ATG9A (red), counterstained for nuclei (DAPI) (blue), and imaged by confocal microscopy. Scale bars: 10 μm. Single-channel images are shown in inverted grayscale with DAPI staining in blue. Images on the rightmost column are fivefold enlargements of the boxed areas in the merge panels. Arrows point to GFP-RUSC2 and ATG9A at vertices of KIF1B-KO cells. Notice that KIF5B KO prevents GFP–RUSC2-induced redistribution to cell vertices. (B) Quantification of the distribution of ATG9A by shell analysis (see scheme in Figure 1D) in KIF1B-KO and KIF5B-KO cells overexpressing GFP-RUSC2 from experiments such as those in panel A. Values are the mean ± SD from the number of cells (n) indicated in the figure from three independent experiments. The statistical significance of the differences was determined using two-way ANOVA followed by Sidak's multiple comparison test. ***$p < 0.001$; ns $p > 0.05$, not significant.

(Figure 4C) contained within the disordered sequence between the RUN and the SH3 domains (Figure 4D). This region lacks canonical W-acidic (i.e., WD or WE) (Dodding *et al.*, 2011) or Y-acidic (i.e., DXYXE/D) (Pernigo *et al.*, 2018) motifs, or CC leucine zipper domains (Cockburn *et al.*, 2018), previously shown to interact with KLCs. From these experiments, we concluded that RUSC2 physically interacts with the KLC2 subunit of kinesin-1, most likely via a novel determinant in the RUSC2 1266–1441 segment.

Interaction of RUSC2 with KLC2 is required for RUSC2-induced redistribution of ATG9A

To obtain a functional correlate for the Y2H analyses, we examined the effect of overexpressing different GFP-RUSC2 truncation mutants on the redistribution of ATG9A to cell vertices (Figure 4E). We found that deletion of the SH3 domain (GFP-RUSC2-1–1466) did not affect the ability of the protein to translocate to cell vertices together with ATG9A (Figure 4, E and F). Further deletion of the disordered region between the RUN and the SH3 domains (GFP-RUSC2-1–1217), however, abolished ATG9A redistribution to cell vertices (Figure 4, E and F). These results were consistent with the interaction of this region with KLC2 (Figure 4, C and D). Taken together, the above experiments demonstrated that interaction of RUSC2 with KLC2 via the RUSC2 1266–1441 disordered segment is essential for the ability of RUSC2 to drive ATG9A toward the cell periphery.

Identification of WDR47 as a RUSC2 interactor

To gain further insight into the mechanism of ATG9A redistribution by RUSC2, we decided to search for other RUSC2 interactors. To this end, we performed affinity purification on anti-tGFP beads of extracts from HeLa cells stably expressing tGFP-RUSC2 or tGFP (nonspecific control) and incubated for 2 h in either complete medium or amino acid- and serum-free HBSS (i.e., starvation) medium (to induce autophagy). Bound proteins were identified by high-performance liquid chromatography-tandem mass spectrometry and analyzed by a label-free quantification method. Differences in protein levels were represented as volcano plots (i.e., scatter plot of significance versus fold change of tGFP-RUSC2 relative to tGFP interactors in triplicate samples) (Figure 5, A and B). Only proteins with adjusted $p < 0.05$ and at least twofold change in abundance were considered hits (Supplemental Table S1). Reassuringly, under both culture conditions, KIF5B and KLC2 (as well as KLC1 under normal culture conditions) were identified as high-scoring RUSC2 interactors (Figure 5, A and B), confirming the functional and physical interactions with kinesin-1 demonstrated in our previous experiments. Interestingly, a top hit in these analyses was WDR47/nemitin (Figure 5, A and B), a WD40-repeat-containing protein previously implicated in brain development, autophagy, and microtubule organization (Wang *et al.*, 2012; Kannan *et al.*, 2017; Chen *et al.*, 2020; Buijs *et al.*, 2021). In agreement with our findings, a recent affinity purification and mass spectrometry analysis of WDR47 interactors conversely identified RUSC2 as a top-10 hit (Chen *et al.*, 2020), although the significance of this interaction was not examined.

Coimmunoprecipitation analyses confirmed the interaction of endogenous WDR47 with tGFP-RUSC2 but not tGFP (Figure 5C). WDR47 was previously predicted to have an α-helical LisH-CTLH domain at its N-terminus and a β-propeller WD40 domain at its C-terminus (Kannan *et al.*, 2017) (Figure 5, D and E). Our bioinformatic analyses predicted two additional folded domains with high probability of α-helices (D1 and D2) downstream of the LisH-CTLH domain and another region with high probability of CCs (CC1-CC2) in the middle of the protein (Figure 5, D and E).

WDR47 inhibits RUSC2-induced ATG9A redistribution to the cell periphery

Next, we assessed the functional significance of the interaction of WDR47 with RUSC2. We observed that mCherry-WDR47 was mostly

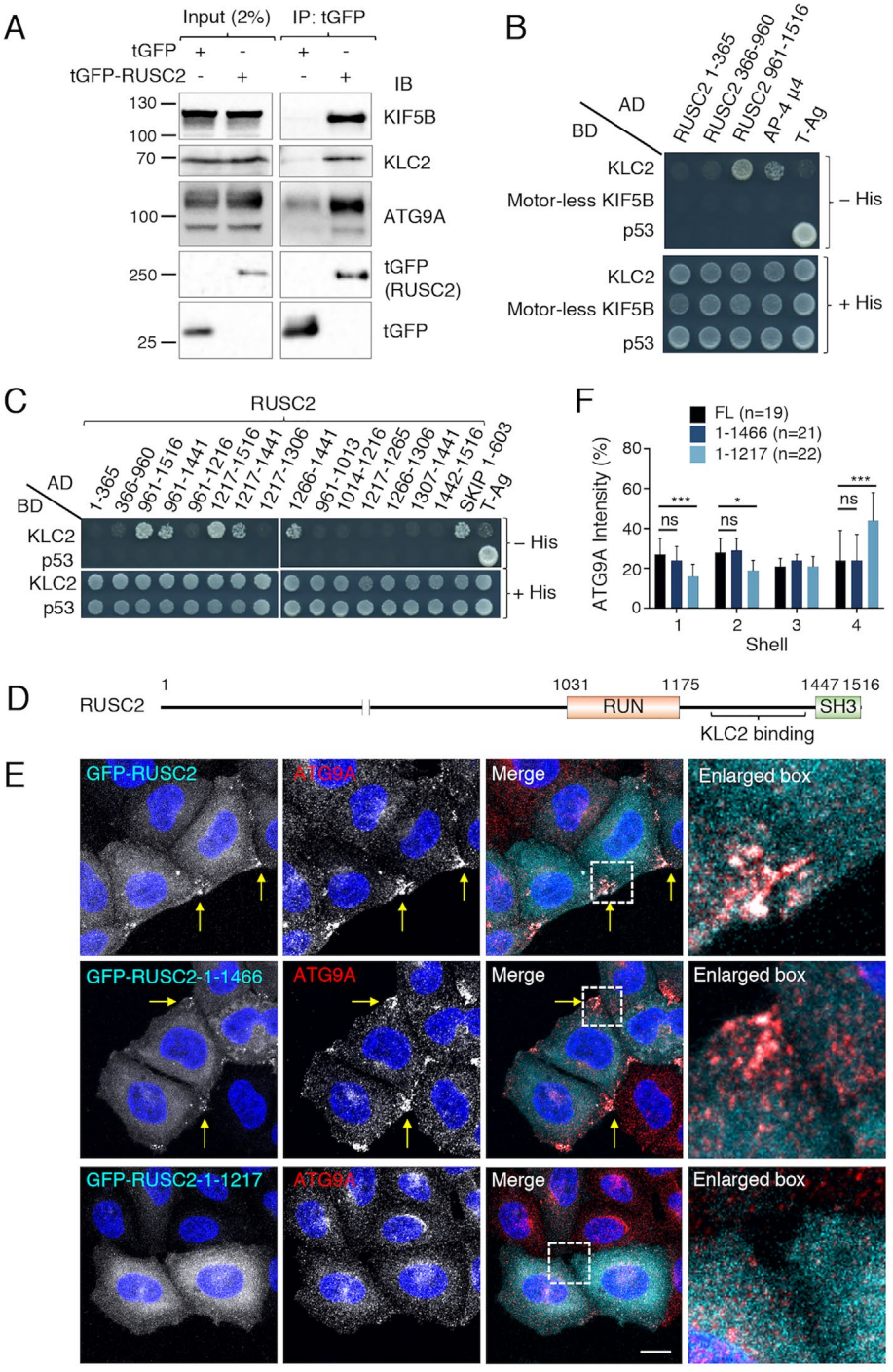

FIGURE 4: Interaction of RUSC2 with KLC2 drives ATG9A to cell vertices. (A) Coimmunoprecipitation of KIF5B, KLC2, and ATG9A with tGFP-RUSC2. Lysates of HeLa cells transfected with plasmids encoding tGFP or tGFP-RUSC2 were subjected to immunoprecipitation (IP) with antibody to the tGFP tag followed by immunoblotting (IB) with antibodies to the indicated proteins. The positions of molecular mass markers (in kDa) are indicated on the left. (B) Y2H analysis of the interaction of Gal4-AD fusions to different fragments of RUSC2, AP–4-μ4 and the SV40 large T antigen (T-Ag) (control) and Gal4-BD fusions to full-length KLC2, motorless KIF5B and p53 (control). Growth in the absence of histidine (–His) is indicative of interactions. Growth in the presence of histidine (+His) is a control for viability and seeding of double transformants. Images shown are representative of three independent experiments. In addition to the interaction of RUSC2 with kinesin-1, the coimmunoprecipitation analyses showed an interaction of RUSC2 with ATG9A (panel A) and the Y2H analyses an interaction of the AP–4-μ4 subunit with KLC2 (panel B). These latter interactions were not further characterized. (C) Y2H analysis of the interaction of 1) a series of RUSC2 fragments, SKIP 1–603 (control), or T-Ag (control) fused to the Gal4 AD with 2) KLC2 or p53 (control) fused to the Gal4 BD. Interactions were assessed as described for panel B. (D) Schematic representation of full-length GFP-RUSC2 indicating the region that interacts with KLC2 (amino acids 1266–1441). (E) HeLa cells were transfected with plasmids encoding GFP-tagged full-length or truncated RUSC2 constructs (cyan), immunostained for endogenous ATG9A (red), counterstained for nuclei (DAPI) (blue), and imaged by confocal microscopy. Scale bars: 10 μm. Single-channel images are shown in inverted grayscale with DAPI staining in blue. Arrows point to GFP-RUSC2 (WT and 1–1466) and ATG9A at vertices of transfected cells. Images on the rightmost column are fivefold enlargements of the boxed areas in the merge panels. (F) Quantification of the distribution of ATG9A by shell analysis (see scheme in Figure 1D) in HeLa cells overexpressing full-length (FL) or truncated forms of GFP-RUSC2. Values are the mean ± SD from the number of cells (n) indicated in the figure in three independent experiments. The statistical significance of the differences was determined using two-way ANOVA followed by Sidak's multiple comparison test. *$p < 0.05$; ***$p < 0.001$; ns $p > 0.05$, not significant.

cytosolic, but a small fraction colocalized with overexpressed GFP-RUSC2 and endogenous ATG9A at cell vertices (Figure 6, arrows). Importantly, CRISPR-Cas9 KO of WDR47 (Figure 7A) increased the proportion of cells with ATG9A and overexpressed GFP-RUSC2 at cell vertices from 31 to 64% (Figure 7, B and C). Moreover, WDR47 KO increased the amount of KIF5B that coimmunoprecipitated with tGFP-RUSC2 relative to WT cells (Figure 7, D and E). These experiments thus demonstrated that WDR47 acts as a negative regulator of RUSC2, inhibiting the ability of RUSC2 to move ATG9A toward the cell periphery through decreased interaction of RUSC2 with kinesin-1.

DISCUSSION

Our studies have thus demonstrated that RUSC2 functions as an adaptor that couples ATG9A vesicles to kinesin-1 for transport from the center to the periphery of the cells. In addition, we have identified WDR47 as a negative regulator of RUSC2. These findings suggest a mechanism for distribution of ATG9A toward the cell periphery, depicted in schematic form in Figure 8. In this mechanism, RUSC2 is recruited to AP–4-coated, ATG9A-containing vesicles budding from the TGN by virtue of interactions with the ear/appendage domains of the ε and β4 subunits of AP-4 (Davies *et al.*, 2018). Once released from the TGN, AP-4 dissociates from the vesicles but RUSC2 remains bound to them. This conclusion is based on the

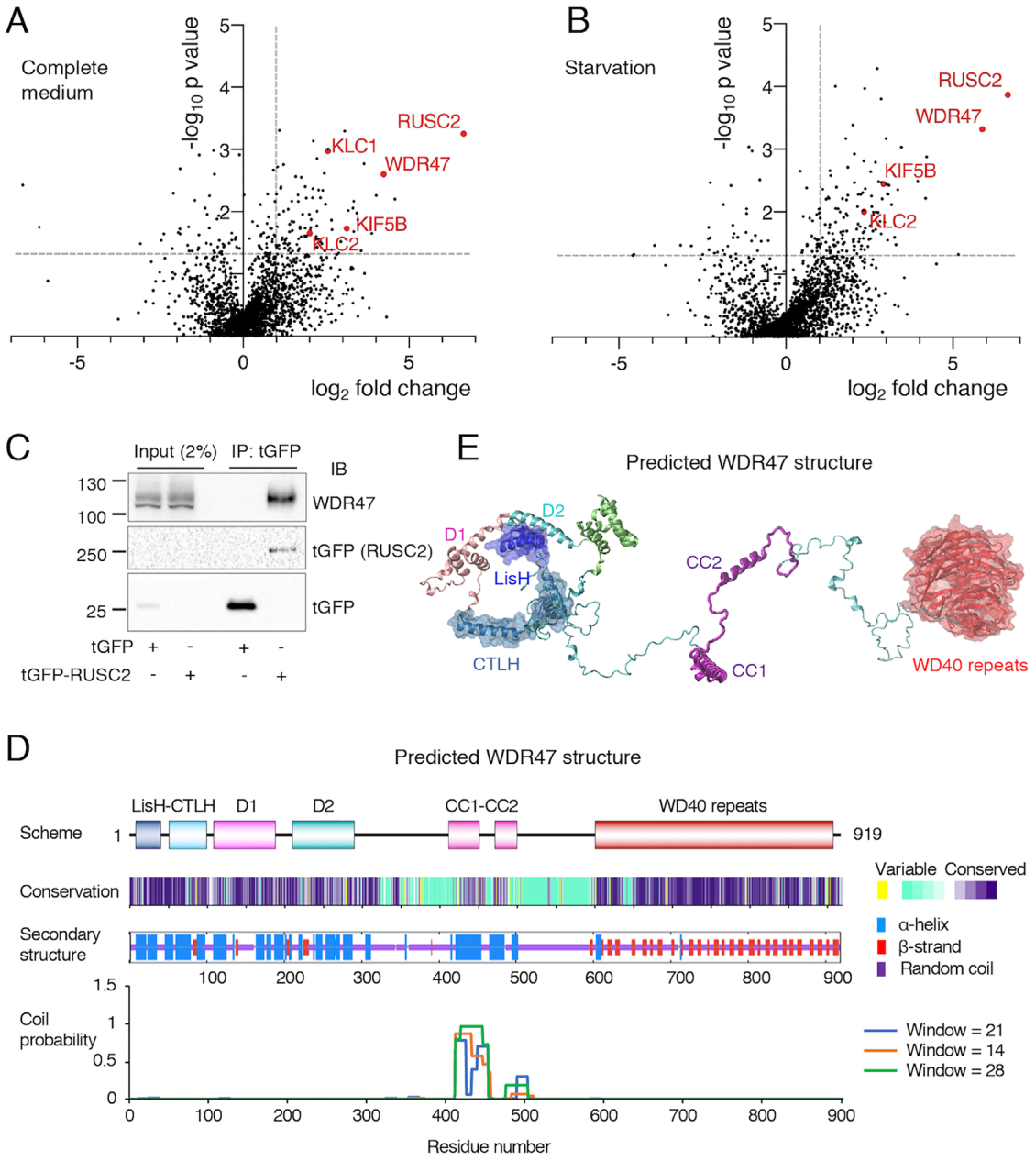

FIGURE 5: Identification of WDR47 as a RUSC2 interactor. (A, B) Volcano plots showing the results of affinity purification and mass spectrometry analysis of RUSC2 interactors from cells cultured for 2 h in complete (A) or starvation (B) medium. Analyses were performed in triplicate. (C) Immunoblot analysis showing coimmunoprecipitation of endogenous WDR47 with tGFP-RUSC2. Lysates of HeLa cells stably transduced with lentiviral plasmids encoding tGFP or tGFP-RUSC2 were immunoprecipitated with antibody to tGFP followed by SDS–PAGE and immunoblotting with antibodies to the indicated proteins. The positions of molecular mass markers are indicated on the left. (D) Domain organization, conservation, secondary structure, and CC prediction of WDR47. Conservation was calculated on the ConSeq server (Berezin *et al.*, 2004) using default search values. Consensus secondary structure prediction was done using the MLRC, DSC and PHD methods at the NPS@ server (https://npsa-prabi.ibcp.fr/cgi-bin/npsa_automat.pl?page=/NPSA/npsa_seccons.html). Coiled coils were predicted using COILS (Lupas *et al.*, 1991). (E) Automated structure prediction of WDR47 by the Robetta server (https://robetta.bakerlab.org/). The known folded LisH-CTLH and WDR40 repeat domains are highlighted as surfaces on the structure. Notice the two predicted folded sequences corresponding to the D1 and D2 domains, and the CCs CC1 and CC2.

observation that AP-4 is required for RUSC2-induced ATG9A redistribution but does not itself redistribute with ATG9A to cell vertices (Davies *et al.*, 2018). Our studies suggest that the persistence of RUSC2 on ATG9A vesicles after dissociation of AP-4 may be due to an interaction of RUSC2 with ATG9A (Figure 4A), although interactions with other components of ATG9A vesicles cannot be ruled out. Peripheral redistribution of ATG9A is then driven by coupling of ATG9A vesicles to kinesin-1 (Figures 2–4), more specifically through an interaction between the disordered region between the RUN and SH3 domains of RUSC2 and the KLC2 subunit of kinesin-1

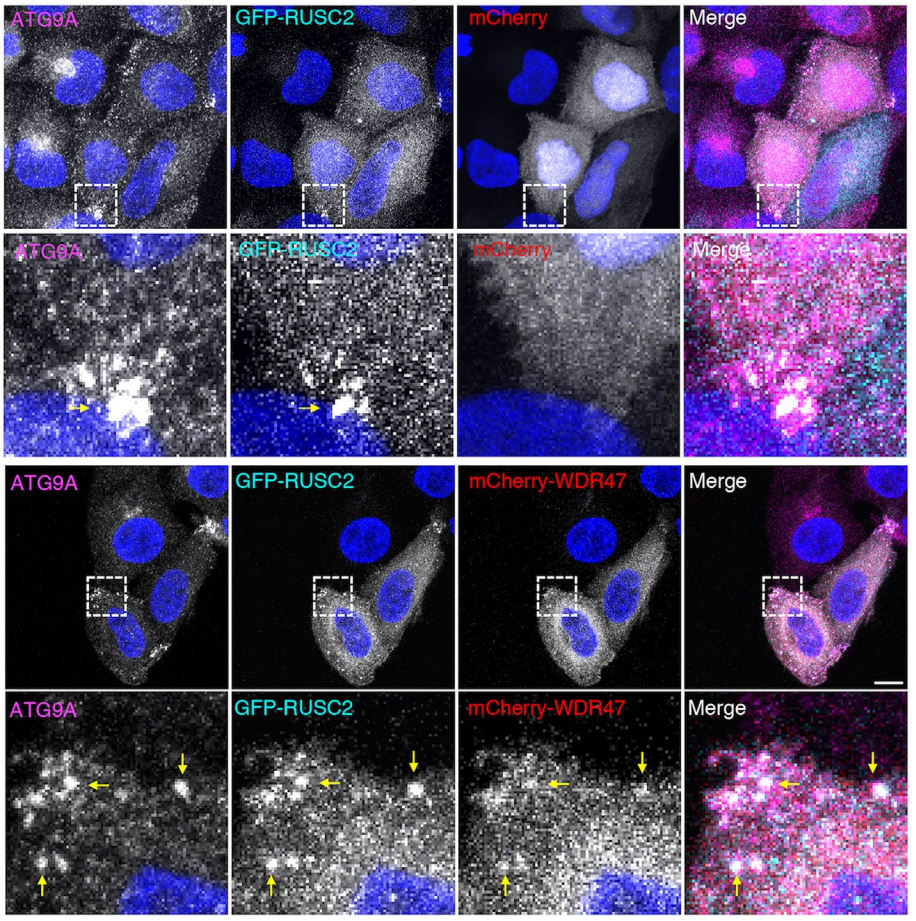

FIGURE 6: Partial colocalization of WDR47 with RUSC2 and ATG9A at cell vertices. HeLa cells were cotransfected with plasmids encoding GFP-RUSC2 (cyan) and mCherry or mCherry-WDR47 (red), immunostained for endogenous ATG9A (magenta), counterstained with DAPI (blue), and imaged by confocal microscopy. Scale bar: 10 µm. Single-channel images are shown in inverted grayscale with DAPI staining in blue. Images in the second and fourth rows are fivefold enlargements of the boxed areas in the first and third rows, respectively. Notice the partial colocalization of mCherry-WDR47 with GFP-RUSC2 and ATG9A at cell vertices (arrows).

(Figure 4, B–D). This mechanism drives transport of ATG9A vesicles toward microtubule plus ends that, in nonpolarized cells such as those used in our studies, are particularly concentrated at cell vertices. WDR47 counters this movement by interacting with RUSC2 and decreasing the binding of RUSC2 to kinesin-1 (Figures 5–7).

Role of kinesin-1 in anterograde transport of ATG9A vesicles.

The identification of kinesin-1 as the motor responsible for RUSC2-mediated anterograde transport of ATG9A was the result of an unbiased screen of all 29 kinesins expressed in Hela cells (Maliga *et al.*, 2013). Remarkably, only silencing of the kinesin-1 heavy chain KIF5B abrogated this transport, whereas silencing of the other kinesins had no effect (Figures 2 and 3; Supplemental Figure S2). In addition to KIF5B and KLC2, specialized cell types express other paralogs of the kinesin-1 heavy chains (KIF5A, KIF5C) and light chains (KLC1, KLC3, and KLC4), and it is possible that combinations of these paralogs will interact with RUSC2 as well. While demonstrating that kinesin-1 mediates RUSC2-dependent movement of ATG9A to the cell periphery, our results do not rule out the involvement of other kinesins in ATG9A transport. It is noteworthy that in *Caenorhabditis elegans* neurons, axonal transport of ATG9 is dependent on the UNC-104 ortholog of mammalian kinesin-3 KIF1B (Stavoe *et al.*, 2016). However, *C. elegans* lacks both AP-4 (Hirst *et al.*, 1999) and RUSC2 (Davies *et al.*, 2018), so it is not surprising that a kinesin other than kinesin-1 is responsible for ATG9 transport in this organism. Further experiments will be needed to assess whether isoforms of kinesin-1 and kinesin-3 mediate transport of ATG9A vesicles in neurons or other specialized cell types.

Our findings add to the growing evidence that kinesin-1 is a major regulator of the autophagy machinery by driving the anterograde transport of lysosomes, autophagosomes, and now ATG9A vesicles. The shared use of kinesin-1 by these organelles allows for their transport along the same microtubule tracks (Guardia *et al.*, 2016), favoring their encounter. However, each of these organelles uses a different adaptor for coupling to kinesin-1: SKIP for lysosomes (Dumont *et al.*, 2010; Rosa-Ferreira and Munro, 2011; Sanger *et al.*, 2017; Keren-Kaplan and Bonifacino, 2021), FYCO1 for autophagosomes (Pankiv *et al.*, 2010; Nieto-Torres *et al.*, 2021), and RUSC2 for ATG9A vesicles (this study). This diversity of adaptors could enable differential control of organelle movement and, thus, spatial regulation of autophagy. Kinesin–1-dependent movement of these organelles also likely contributes to the distribution of autophagic function to the peripheral cytoplasm. The importance of this distribution is underscored by the demonstrated autophagic dysfunction in nonneuronal cells defective in SKIP (Muhammad *et al.*, 2015), FYCO1 (Olsvik *et al.*, 2015), or RUSC2 (Davies *et al.*, 2018). We anticipate that the movement of autophagy-related organelles will be even more important in cells that are highly dependent on long-range organelle transport such as neurons.

A novel determinant for adaptor binding to KLC2?

Molecular dissection of RUSC2 revealed that binding to KLC2 depends on the disordered region that connects the RUN and SH3 domains (amino acids 1266–1441) (Figure 4). This region lacks canonical W-acidic or Y-acidic motifs previously shown to mediate interactions of other adaptors with KLCs (Dodding *et al.*, 2011; Pernigo *et al.*, 2018). Determinants other than W-acidic and Y-acidic motifs have also been shown to mediate interaction of adaptors with KLCs through binding to different sites. For example, whereas W-acidic and Y-acidic motifs bind to partially overlapping sites on the concave surface of a single KLC tetratricopeptide repeat (TPR) domain (Pernigo *et al.*, 2013, 2018), CC leucine zipper domains from two JIP3 proteins bind end-on to TPRs from two copies of KLC2 (Cockburn *et al.*, 2018). The COILS server (https://embnet.vital-it.ch/software/COILS_form.html) does not predict CCs in the 1266–1441 region of RUSC2, so the KLC-binding determinant must also be different from that in JIP3. Further work will be needed to precisely delineate the RUSC2 determinant. In any event, our

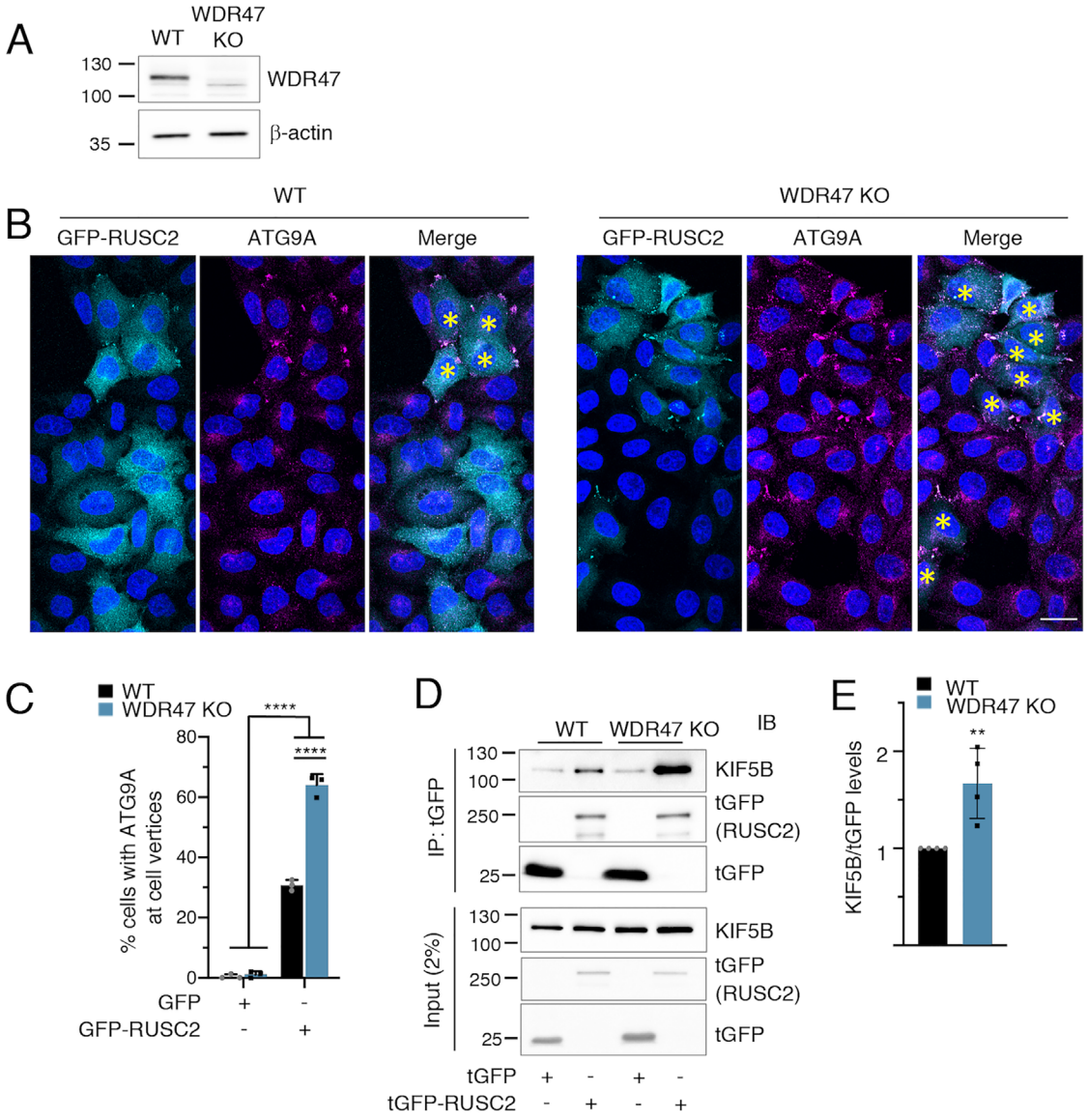

FIGURE 7: WDR47 depletion enhances RUSC2-induced redistribution of ATG9A to cell vertices. (A) Immunoblot analysis of WDR47-KO HeLa cells. The positions of molecular mass larkers (in kDa) are indicated at left. (B) WT or WDR47-KO HeLa cells were transfected with plasmids encoding GFP-tagged RUSC2 (cyan), immunostained for endogenous ATG9A (magenta), counterstained with DAPI (blue), and imaged by confocal microscopy. Scale bars: 10 μm. Asterisks indicate transfected cells with GFP-RUSC2 and ATG9A at vertices. (C) Quantification of the percentage of cells with ATG9A at cell vertices in WT and WDR47-KO HeLa cells overexpressing either GFP or GFP-RUSC2. Values are the mean ± SD from at least 100 cells per sample in three independent experiments. The statistical significance of the differences was determined using two-way ANOVA followed by Tukey's multiple comparison test. ****$p < 0.0001$. Notice the increase in the proportion of cells with ATG9A at vertices of WDR47-KO cells. (D) Immunoblot analysis showing increased coimmunoprecipitation of KIF5B with tGFP-RUSC2 in WDR47-KO compared with WT cells. Lysates of WT or WDR47-KO HeLa cells transfected with plasmids encoding tGFP or tGFP-RUSC2 were immunoprecipitated using antibody to tGFP followed by SDS–PAGE and immunoblotting with antibodies to endogenous KIF5B. The positions of molecular mass markers (in kDa) are indicated on the left. (E) Quantification of the blots from the coimmunoprecipitation experiment shown in panel D. Values represent levels of KIF5B relative to coimmunoprecipitated tGFP-RUSC2 after subtraction of background KIF5B from the tGFP control lanes. Values are the mean ± SD from four independent experiments. The statistical significance of the differences was determined using Student's *t* test. **$p < 0.01$.

findings add to the diversity of KLC-binding determinants used by different kinesin-1 adaptors. Adaptors such as SKIP (Sanger *et al.*, 2017) and JIP3 (Watt *et al.*, 2015) can also bind to the tail domain of the kinesin-1 heavy chain, triggering its conformational activation. In the case of RUSC2, however, we did not detect an interaction with motorless KIF5B (Figure 4B), indicating a different mechanism.

Inhibition of RUSC2 function by WDR47

In addition to demonstrating that RUSC2 functions as a kinesin-1 adaptor, our studies identified WDR47 as an inhibitor of this function. Indeed, KO of WDR47 increases interaction of RUSC2 with kinesin-1 and enhances RUSC2-induced redistribution of ATG9A to cell vertices (Figure 7). WDR47 is likely to exert this effect in association with

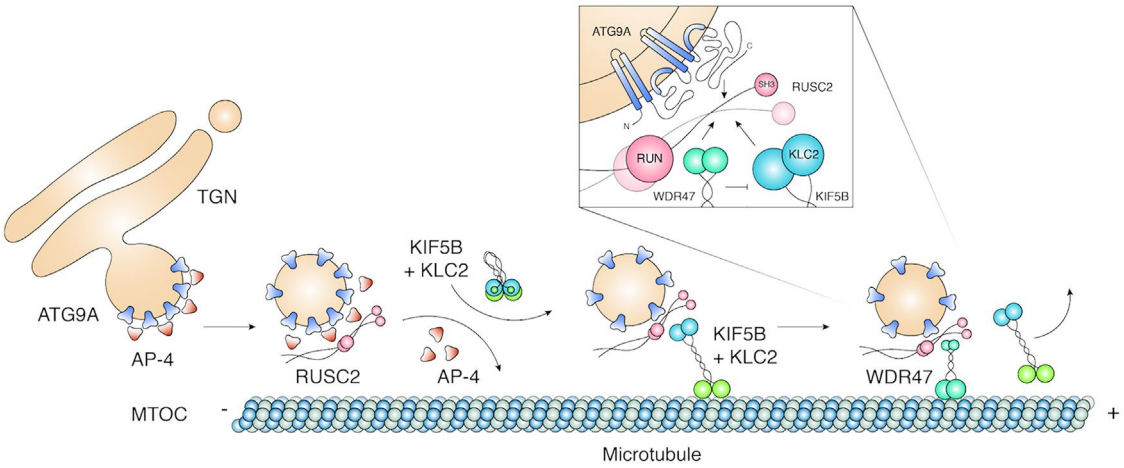

FIGURE 8: Proposed mechanism of transport of ATG9A-containing vesicles to the cell periphery. ATG9A is sorted into ATG9A vesicles by interaction of its N-terminal cytosolic domain with the μ4 subunit of AP-4 (Mattera *et al.*, 2017). RUSC2 binds to AP-4 (Davies *et al.*, 2018) and recruits kinesin-1 via interaction of its second disordered domain within KLC2 (this study). AP-4 dissociates from ATG9A vesicles (before or after kinesin-1 recruitment), but RUSC2 remains bound to the vesicles (Davies *et al.*, 2018), possibly via interaction with ATG9A (this study). Kinesin-1 drives ATG9A vesicles toward the cell periphery (this study), likely for delivery to PAS or endosomes. WDR47 interacts with RUSC2, reducing the coupling to kinesin-1 and impairing movement of ATG9A vesicles toward the cell periphery (this study). This system allows for the regulated distribution of ATG9A toward the cell periphery. RUSC2 and WDR47 are shown as dimers for symmetry with kinesin-1, although there is currently no evidence for the dimerization of these proteins.

microtubules, as previous studies showed that it binds to microtubules via the microtubule-associated proteins MAP8 (also known as MAP1S) (Wang *et al.*, 2012) and CAMSAPs (Chen *et al.*, 2020; Buijs *et al.*, 2021), and that it participates in microtubule-dependent processes such as neural stem cell proliferation, radial migration, growth cone dynamics, and neuronal polarization (Kannan *et al.*, 2017; Chen *et al.*, 2020). Thus, RUSC2, kinesin-1, and WDR47 share the property of direct or indirect association with microtubules, providing the right spatial context for their functional interactions.

WDR47 shares with the lissencephaly protein LIS1 the property of having an N-terminal LisH domain and a C-terminal WD40-repeat domain (Wang *et al.*, 2012). Since LIS1 is a well-known regulator of dynein motor activity (Markus *et al.*, 2020), WDR47 could also oppose RUSC2 function by activating dynein–dynactin-mediated retrograde transport of ATG9A vesicles. However, this retrograde transport was previously shown to be mediated by coupling of AP-4/ATG9A-containing vesicles to dynein-dynactin by the FHF complex (Mattera *et al.*, 2020). It would therefore be of interest to determine whether WDR47 also interacts with dynein-dynactin and FHF.

RUSC2 and WDR47 also modulate autophagy, albeit in different ways. RUSC2 KD was shown to decrease the ratio of LC3B-II to LC3B-I, indicative of a defect in autophagosome formation or maturation (Davies *et al.*, 2018). In contrast, WDR47 KD increased autophagic flux, suggesting that WDR47 is a negative regulator of autophagy (Kannan *et al.*, 2017). It is tempting to speculate that these opposite effects on autophagy are related to the negative regulatory activity of WDR47 on RUSC2 for the transport of ATG9A-containing vesicles (Figure 8).

Disease connections

Loss-of-function mutations in RUSC2 have been shown to cause a human neurodevelopmental disorder characterized by hypotonia, microcephaly, intellectual disability, and seizures (OMIM entry #617773) (Alwadei *et al.*, 2016). The reported mutations include the biallelic nonsense substitutions c.2596C>T and c.3952C>T, which result in proteins with C-terminal truncations of the entire RUN-disordered-SH3 region (pArg866*), or part of the disordered region and the SH3 domain (pArg1318*), respectively (Alwadei *et al.*, 2016). Based on our deletion analysis (Figure 4), both truncations could affect the ability of RUSC2 to couple ATG9A vesicles to kinesin-1.

The disease caused by RUSC2 mutations in many ways resembles the complicated from of HSP caused by mutations in AP-4 subunit genes (i.e., AP–4-deficiency syndrome) (OMIM entries #614055, 612936, 613744, 614067) (Verkerk *et al.*, 2009; Abou Jamra *et al.*, 2011; Behne *et al.*, 2020). Both RUSC2- and AP–4-mutant patients feature hypoplasia of the corpus callosum (Verkerk *et al.*, 2009; Abou Jamra *et al.*, 2011; Alwadei *et al.*, 2016; Behne *et al.*, 2020), a structure composed of myelinated axons that connect the two brain hemispheres. These similarities are consistent with the involvement of both RUSC2 and AP-4 in mobilizing ATG9A to peripheral locations and suggest that failure of ATG9A mobilization may be a key element in the pathogenesis of the disease.

Mutations in WDR47 have not yet been shown to cause disease in humans. However, hypomorphic or complete loss-of-function mutations of WDR47 in mice result in lethality over the first few months of life in association with various neurodevelopmental defects, including microcephaly and agenesis of the corpus callosum (Kannan *et al.*, 2017). These features are somewhat similar to those of RUSC2- and AP–4-mutant patients (Verkerk *et al.*, 2009; Abou Jamra *et al.*, 2011; Alwadei *et al.*, 2016; Behne *et al.*, 2020) and AP–4-mutant mice (Matsuda *et al.*, 2008; De Pace *et al.*, 2018; Ivankovic *et al.*, 2020). However, the defects in WDR47-mutant mice are more severe, suggesting that WDR47 does more than just regulate the interaction of RUSC2 with kinesin-1. This suggestion is supported by the fact that WDR47 is present in organisms such as *C. elegans* and *Drosophila melanogaster* (Wang *et al.*, 2012), which lack AP-4 and RUSC2 (Hirst *et al.*, 1999; Davies *et al.*, 2018), and that WDR47 regulates other microtubule-dependent processes (Wang *et al.*, 2012; Chen *et al.*, 2020; Buijs *et al.*, 2021).

Concluding remarks

Our findings have thus uncovered a novel mechanism for the regulated coupling of a membrane-bound organelle to a kinesin for anterograde transport along microtubules. The mechanism involves RUSC2-mediated coupling of ATG9 vesicles to kinesin-1 and an inhibitory effect of WDR47 on this coupling. These findings highlight a role for AP-4 in kinesin-1 recruitment, in addition to its better-known role in cargo sorting. AP-4 can also recruit dynein-dynactin via the FHF complex (Mattera *et al.*, 2020). The ability of AP-4 to couple to both kinesin-1 and dynein-dynactin enables bidirectional movement of AP–4-coated vesicles, ensuring distribution of the vesicles and their content to different regions of the cell.

MATERIALS AND METHODS

Plasmid constructs

Human RUSC2 cDNA was obtained from the ORFeome v8.1 collection (GE Dharmacon, RUSC2: MHS6278-202800194) and subcloned into the pGFP-C1 vector (Clontech, Takara Bio) encoding a monomeric GFP variant (A206K). The cDNA was also subcloned into the pLKO.1 plasmid encoding a puromycin-resistant cassette and a tGFP fluorescent tag upstream of the multiple cloning site to generate the tGFP-RUSC2 construct for lentivirus delivery. Additional plasmids psPAX2 (Addgene #12260), pMD2.G (Addgene #12259), and pAdVantage (Promega, E1711) were used for lentivirus production. Plasmids encoding GFP-RUSC2 mutants were generated by PCR and subsequent subcloning of the different sequences of interest into the pGFP(A206K)-C1 vector. Human WDR47 cDNA (GE Dharmacon, MHS6278-202807085) was subcloned into the pmCherry-C1 empty vector (Clontech, Takara Bio). Plasmids encoding GFP-KIF5B and HA-KLC2 were previously described (Guardia *et al.*, 2016). Constructs for Y2H studies encoding several fragments of human RUSC2, motorless mouse KIF5B (326–963), full-length human KLC2 (Guardia *et al.*, 2016), and truncated human SKIP (1–603) (Dodding *et al.*, 2011; Pernigo *et al.*, 2013) were amplified by PCR and cloned into the Gal4 AD or BD vectors pGADT7 and pGBT9 (Clontech), respectively. Human AP–4-μ4 cDNA subcloned into the Gal4 AD vector pACT2 (Clontech, Takara Bio) was previously described (Guo *et al.*, 2013). The BD-p53 and AD-T-Ag control constructs were obtained from Clontech, Takara Bio. The sequence of all constructs was confirmed by Sanger sequencing (Eurofins).

siRNAs

The following siRNAs (ON-TARGETplus SMART-pools) (GE Dharmacon) were used in our experiments: nontargeting (#D-001810-10-20), KIF11 (L-003317-00-0005), KIF13A (L-008257-00-0005), KIF13B (L-004963-00-0005), KIF14 (L-003319-00-0005), KIF15 (L-004960-00-0005), KIF16B (L-009495-00-0005), KIF18A (L-006849-00-0005), KIF18B (L-010460-01-0005), KIF1B (L-009317-00-0005), KIF1C (L-010354-00-0005), KIF20B (L-003318-00-0005), KIF21A (L-004969-00-0005), KIF22 (L-004962-00-0005), KIF23 (L-004956-00-0005), KIF24 (L-010459-02-0005), KIF26A (L-022010-00-0005), KIF2A (L-004959-00-0005), KIF2C (L-004955-00-0005), KIF3A (L-004964-00-0005), KIF3B (L-009595-00-0005), KIF3C (L-009469-00-0005), KIF4A (L-004961-00-0005), KIF4B (L-004965-01-0005), KIF5B (L-008867-00-0005), KIF7 (L-022322-01-0005), KIF9 (L-004967-00-0005), KIFC1 (L-004958-00-0005), KIFC2 (L-008786-00-0005), and KIFC3 (L-008338-00-0005).

Antibodies

The following antibodies were used in this study: rabbit anti-ATG9A (Abcam, ab108338; 1:200 for IF; 1:1000 for IB), mouse anti-β-actin (Applied Biological Materials, G043; 1:2,000 for IB), rabbit anti-KIF5B (Abcam, ab167429; 1:2,000 for IB), rabbit anti-KIF1B (Bethyl Laboratories Inc., A301-055A; 1:1000 for IB), mouse anti-LAMP1 (Developmental Studies Hybridoma Bank, H4A3; 1:1000 for IF), rabbit anti-KLC2 (a mixture of two antibodies: Thermo Fisher Scientific, PA5-59168 and Abcam, ab95881; both at 1:1000 for IB), mouse anti-tGFP (Origene, TA150041; 1:1000 for IB), chicken anti-HA (influenza hemagglutinin) epitope tag (Millipore Sigma, AB3254; 1:250 for IF), rabbit anti-WDR47 (Abcam, ab121935; 1:1000 for IB), Alexa Fluor 488–conjugated donkey anti-rabbit IgG (Thermo Fisher, A-21206; 1:1000 for IF), Alexa Fluor 488–conjugated donkey anti-mouse IgG (Thermo Fisher, A-21202; 1:1000 for IF), Alexa Fluor 555–conjugated donkey anti-rabbit IgG (Thermo Fisher, A-31572; 1:1000 for IF), Alexa Fluor 555–conjugated donkey anti-mouse IgG (Thermo Fisher, A-31570; 1:1000 for IF), Alexa Fluor 647–conjugated goat anti-chicken IgY (Thermo Fisher, A-21449; 1:1000 for IF), HRP–conjugated goat anti-rabbit IgG (H+L) (Jackson ImmunoResearch, 111-035-003; 1:5,000 for IB), and HRP–conjugated donkey anti-mouse IgG (H+L) (Jackson ImmunoResearch, 715-035-150; 1:5,000 for IB).

Cell culture, transfection, and lentivirus production

HeLa and HEK293T cells (ATCC) were grown in DMEM (Quality Biological, 112-319-101) supplemented with 10% fetal bovine serum (Corning, 35-011-CV) and 100 U/ml penicillin, 100 μg/ml streptomycin (Corning, 30002-CL) (complete DMEM) at 37°C and 95% air:5% CO_2.

For immunofluorescence imaging, HeLa cells on 12-mm glass coverslips (Thermo Fisher Scientific, 12 545 80P) in 24-well dishes (Corning) were transfected with 1.0–2.5 μg plasmids and 1.5 μl Lipofectamine 2000 (Thermo Fisher Scientific, 11668027) according to the manufacturer's protocol. Transfection of HEK293T cells for lentivirus production was conducted in the same manner but in 6-well dishes without coverslips. DNA (0.8 μg psPAX2, 0.3 μg pMD2.G, 0.1 μg pAdVantage, and 1.2 μg tGFP or tGFP-RUSC2) and Lipofectamine 3000 (Thermo Fisher Scientific, L3000015) were used according to the manufacturer's protocol. Following a 18-h incubation, the medium was changed to 3 ml complete DMEM supplemented with ViralBoost reagent (Alstem, VB100). After 2 d of incubation, the supernatant was collected, and the cell debris was spun out at 700 × *g* for 5 min at 4°C. The virus suspension was immediately used for lentiviral transduction of HeLa cells.

HeLa cells stably transduced with tGFP or tGFP-RUSC2 lentivirus were selected by the addition of 1 μg/ml puromycin (Thermo Fisher Scientific, A1113803) to the culture medium 4 d after infection. Individual clones were isolated approximately 1 wk after the initial transduction by selecting tGFP-positive cells in a FACSAria II sorter (BD Biosciences), grown on 96-well plates, and analyzed by immunofluorescence and immunoblotting using anti-tGFP.

For KD experiments, HeLa cells were transfected with 25 nM siRNA and 1.0 μl of Lipofectamine 2000 according to the manufacturer's protocol, split onto coverslips ~24 h later, and transfected again the next day following the same protocol but including GFP-RUSC2 plasmid. Cells were analyzed 24 h after the second transfection (i.e., ~72 h after the first transfection).

CRISPR-Cas9 knock-out

WDR47-KO and RUSC2-KO HeLa cells were generated using CRISPR-Cas9 (Cong *et al.*, 2013). We used a single gRNA (AGAAACAGTGAATGTAAAAG sequence) to target a PAM sequence in Exon 1 of the *WDR47* gene and a pair of targeting gRNAs (GTCCTAGGTCTTGATCGGGC and GGGGGATGTGATGAACGATG sequences) to remove ~125 bp from Exon 1 of the *RUSC2*

gene. Complementary gRNAs were annealed and subcloned into the pSpCas9(BB)-2A-GFP (pX-458) vector (Addgene plasmid #48138) between BbsI endonuclease restriction sites. HeLa cells were transfected with plasmids encoding the different gRNAs using Lipofectamine 2000 and the protocols mentioned above. At 48 h after transfection, GFP-positive cells were sorted in a FACSAria II and single clones were collected in 96-well plates. After 14 d, colonies were expanded, and cells were analyzed. Positive colonies were verified by immunoblotting with antibody to endogenous WDR47 or PCR of RUSC2 genomic DNA with the following primers: Forward: 5′-GGGCATGCCCCTGACTTCCAGGGAG-3′ and Reverse: 5′-CACCAAGTCCTGGCTCACCCACACC-3′. AP4E1-, KIF5B- and KIF1B-KO HeLa cells were previously described (Jia *et al.*, 2017; Mattera *et al.*, 2017).

Y2H analysis

Transformation of the AH109 yeast reporter strain with BD and AD plasmids and plate selection were performed as previously described (Mattera *et al.*, 2003). Briefly, cotransformation of the AH109 yeast reporter strain (auxotroph for adenine, histidine, leucine, and tryptophan) with AD and BD plasmids (conferring ability to survive in medium lacking leucine or tryptophan, respectively) and isolation of double transformants were performed according to the guidelines in the Matchmaker two-hybrid system manual (Clontech, Takara Bio). Cotransformation of AD constructs with BD-p53 and of BD-constructs with AD-T-Ag provided a negative control, whereas the AD-T-Ag/BD-p53 double transformant was used as a positive control (Mattera *et al.*, 2003). Interaction between AD- and BD-fusion proteins, resulting in activation of the *HIS3* reporter gene, was assessed in plates lacking histidine, leucine, and tryptophan (–His). Plating on medium lacking only leucine and tryptophan (+His) provided a control for viability and seeding of the double transformants. Colonies were scanned following 2–4 d of incubation at 30°C.

Coimmunoprecipitation assays

For coimmunoprecipitation of tGFP or tGFP-RUSC2 with endogenous ATG9A, KIF5B, KLC2, and WDR47, stably transduced cell lines were plated on a 10-cm dish and cultured to 90% confluency. Cells were harvested with a cell scraper, collected in a tube, washed three times in ice-cold phosphate-buffered saline (PBS) and pelleted each time by centrifugation (3 min at 500 × *g* and 4°C). Cell pellets were resuspended in 200 µl ice-cold lysis buffer (10 mM Tris, pH 7.5, 150 mM NaCl, 0.5 mM EDTA, 0.5% NP-40) supplemented with complete EDTA-free protease inhibitors (Roche, 11873580001) and 1 mM PMSF at 4°C for 30 min with occasional mixing. The soluble fraction was separated by centrifugation for 10 min at 20,000 × *g* and 4°C. Samples were diluted with wash buffer (10 mM Tris/HCl, pH 7.5, 150 mM NaCl, 0.5 mM EDTA), incubated on 20 µl tGFP-Trap magnetic agarose beads (ChromoTek, tbtma-20), and processed according to the manufacturer's protocol. Immunoprecipitates were eluted by heating for 10 min at 99°C with 1× Laemmli Sample Buffer (Bio-Rad, 1610747) and analyzed by SDS–PAGE and immunoblotting or mass spectrometry.

Mass spectrometry

Samples were loaded on 1-mm Any kD precast polyacrylamide gels (Bio-Rad). Bands containing the entire sample were cut. Samples were reduced with 10 mM TCEP for 1 h, alkylated with 10 mM NEM for 10 min, and digested with trypsin at 37°C overnight. Peptides were extracted from the gel and desalted using Oasis HLB µElution plates (Waters). Digests of each sample were injected into an Ultimate 3000 RSLC nano HPLC system (Thermo Fisher Scientific). Peptides were separated on an ES802 column over a 63-min gradient with mobile phase B (98% acetonitrile, 1.9% H_2O, 0.1% formic acid) increased from 3 to 24%. LC-MS/MS data were acquired on an Orbitrap Lumos mass spectrometer (Thermo Fisher Scientific) in data-dependent acquisition mode. The MS1 scans were performed in Orbitrap with a resolution of 120 K, a mass range of 375–1500 m/z, and an AGC target of 2×10^5. The quadrupole isolation was used with a window of 1.5 m/z. The MS/MS scans were triggered when the intensity of precursor ions with a charge state between 2 and 6 reached 1×10^4. The MS2 scans were conducted in an ion trap. The CID method was used with collision energy fixed at 30%. The instrument was run in top speed mode. MS1 scan was performed every 3 s, and as many MS2 scans were acquired within the 3-s cycle.

The database search and label-free quantification were performed using Proteome Discoverer 2.2 software. Up to two missed cleavages were allowed for trypsin digestion. NEM on cysteines and oxidation on methionine were set as fixed and variable modifications, respectively. Mass tolerances for MS1 and MS2 scans were set to 5 ppm and 0.6 Da, respectively. The search results were filtered by a false discovery rate of 1% at the protein level. The summed intensity of the unique peptides was used for protein ratio calculation. The missing values were inputted. The maximum and minimum fold changes allowed were set to 100 and 0.01, respectively. The total peptide amount of each sample was used for normalization. The individual protein ANOVA method was used for hypothesis test. Proteins with log2 fold change ≥ or ≤ –1 and adjusted *p* value ≤ 0.05 were considered significantly changed.

Fluorescence microscopy

At 24 h after transfection, HeLa cells were washed with PBS and treated for 12 min with 4% paraformaldehyde (Electron Microscopy Sciences, 15714-S) in PBS. Coverslips were washed twice for 5 min in PBS and permeabilized for 15 min in 0.2% Triton X-100 (Sigma, T8787). Cells were blocked for 30 min in 0.2% bovine serum albumin (GoldBio, A-421) in PBS (blocking solution) and stained for 30 min with primary antibodies in blocking solution at 37°C. Coverslips were then washed twice with PBS and incubated for 30 min at 37°C with secondary Alexa–conjugated antibodies in blocking solution. Coverslips were again washed twice with PBS and mounted on slides using Fluoromount-G with DAPI (Electron Microscopy Sciences, 17984-24). Images were acquired on an inverted confocal laser-scanning microscope (LSM780; Carl Zeiss) fitted with a 63×, 1.4 NA objective. Images were processed in ImageJ (Schneider *et al.*, 2012).

Shell analysis for measurement of particle distribution

To quantify the distribution of ATG9A, cells with a relatively round shape were chosen for analysis, since other cell shapes could not be quantified accurately. Cell outlines were traced in ImageJ and the total fluorescence signal was measured. The cell outline was iteratively shrunken by 2 µm (*Edit* > *Selection* > *Enlarge*… plugin) to produce a total of 4 "shells", 1 being the most peripheral and 4 being the perinuclear region of the cell, and the signal within each shell was measured. Intensity values for each shell were calculated relative to the total intensity in the cell and expressed as a percentage of the total.

Quantification and statistics

Data were analyzed in Prism version 8.3.1 (GraphPad Software). Experimental replicates, as well as the test applied to compute statistical significance between different conditions, are described in each figure legend.

ACKNOWLEDGMENTS

We thank Xiaolin Zhu and Boma Fubara for expert technical assistance; Amra Saric, Raffaella De Pace, and Tal-Keren-Kaplan for critical review of the manuscript; and other members of the Bonifacino laboratory for helpful discussions. This project was funded by the Intramural Program of the Eunice Kennedy Shriver National Institute of Child Health and Human Development, National Institutes of Health (Project # ZIA HD001607).

REFERENCES

Abou Jamra R, Philippe O, Raas-Rothschild A, Eck SH, Graf E, Buchert R, Borck G, Ekici A, Brockschmidt FF, Nöthen MM, *et al.* (2011). Adaptor protein complex 4 deficiency causes severe autosomal-recessive intellectual disability, progressive spastic paraplegia, shy character, and short stature. Am J Hum Genet 88, 788–795.

Alwadei AH, Benini R, Mahmoud A, Alasmari A, Kamsteeg E-J, Alfadhel M (2016). Loss-of-function mutation in RUSC2 causes intellectual disability and secondary microcephaly. Dev Med Child Neurol 58, 1317–1322.

Bayer M, Fischer J, Kremerskothen J, Ossendorf E, Matanis T, Konczal M, Weide T, Barnekow A (2005). Identification and characterization of Iporin as a novel interaction partner for rab1. BMC Cell Biol 6, 15.

Behne R, Teinert J, Wimmer M, D'Amore A, Davies AK, Scarrott JM, Eberhardt K, Brechmann B, Chen IP, Buttermore ED, *et al.* (2020). Adaptor protein complex 4 deficiency: a paradigm of childhood-onset hereditary spastic paraplegia caused by defective protein trafficking. Hum Mol Genet 29, 320–334.

Bejarano E, Murray JW, Wang X, Pampliega O, Yin D, Patel B, Yuste A, Wolkoff AW, Cuervo AM (2018). Defective recruitment of motor proteins to autophagic compartments contributes to autophagic failure in aging. Aging Cell 17, e12777.

Bento CF, Renna M, Ghislat G, Puri C, Ashkenazi A, Vicinanza M, Menzies FM, Rubinsztein DC (2016). Mammalian autophagy: How does it work? Annu Rev Biochem 85, 685–713.

Berezin C, Glaser F, Rosenberg J, Paz I, Pupko T, Fariselli P, Casadio R, Ben-Tal N (2004). ConSeq: the identification of functionally and structurally important residues in protein sequences. Bioinformatics 20, 1322–1324.

van Bergeijk P, Hoogenraad CC, Kapitein LC (2016). Right time, right place: Probing the functions of organelle positioning. Trends Cell Biol 26, 121–134.

Bielska E, Schuster M, Roger Y, Berepiki A, Soanes DM, Talbot NJ, Steinberg G (2014). Hook is an adapter that coordinates kinesin-3 and dynein cargo attachment on early endosomes. J Cell Biol 204, 989–1007.

Bonifacino JS, Neefjes J (2017). Moving and positioning the endolysosomal system. Curr Opin Cell Biol 47, 1–8.

Buijs RR, Hummel JJA, Burute M, Pan X, Cao Y, Stucchi R, Altelaar M, Akhmanova A, Kapitein LC, Hoogenraad CC (2021). WDR47 protects neuronal microtubule minus ends from katanin-mediated severing. Cell Rep 36, 109371.

Cason SE, Carman PJ, Van Duyne C, Goldsmith J, Dominguez R, Holzbaur ELF (2021). Sequential dynein effectors regulate axonal autophagosome motility in a maturation-dependent pathway. J Cell Biol 220, e202010179.

Chen Y, Zheng J, Li X, Zhu L, Shao Z, Yan X, Zhu X (2020). Wdr47 controls neuronal polarization through the camsap family microtubule minus-end-binding proteins. Cell Rep 31, 107526.

Cockburn JJB, Hesketh SJ, Mulhair P, Thomsen M, O'Connell MJ, Way M (2018). Insights into kinesin-1 activation from the crystal structure of KLC2 bound to JIP3. Structure 26, 1486–1498.e6.

Cong L, Ran FA, Cox D, Lin S, Barretto R, Habib N, Hsu PD, Wu X, Jiang W, Marraffini LA, *et al.* (2013). Multiplex genome engineering using CRISPR/Cas systems. Science 339, 819–823.

Coy DL, Hancock WO, Wagenbach M, Howard J (1999). Kinesin's tail domain is an inhibitory regulator of the motor domain. Nat Cell Biol 1, 288–292.

Davies AK, Itzhak DN, Edgar JR, Archuleta TL, Hirst J, Jackson LP, Robinson MS, Borner GHH (2018). AP-4 vesicles contribute to spatial control of autophagy via RUSC-dependent peripheral delivery of ATG9A. Nat Commun 9, 3958.

Dell'Angelica EC, Mullins C, Bonifacino JS (1999). AP-4, a novel protein complex related to clathrin adaptors. J Biol Chem 274, 7278–7285.

Dodding MP, Mitter R, Humphries AC, Way M (2011). A kinesin-1 binding motif in vaccinia virus that is widespread throughout the human genome. EMBO J 30, 4523–4538.

Drerup CM, Nechiporuk AV (2013). JNK-interacting protein 3 mediates the retrograde transport of activated c-jun N-terminal kinase and lysosomes. PLOS Genet 9, e1003303.

Dumont A, Boucrot E, Drevensek S, Daire V, Gorvel J-P, Poüs C, Holden DW, Méresse S (2010). SKIP, the host target of the Salmonella virulence factor SifA, promotes Kinesin–1-dependent vacuolar membrane exchanges. Traffic 11, 899–911.

Fu M-M, Nirschl JJ, Holzbaur ELF (2014). LC3 binding to the scaffolding protein JIP1 regulates processive dynein-driven transport of autophagosomes. Dev Cell 29, 577–590.

Ghanbarpour A, Valverde DP, Melia TJ, Reinisch KM (2021). A model for a partnership of lipid transfer proteins and scramblases in membrane expansion and organelle biogenesis. Proc Natl Acad Sci USA 118, e2101562118.

Gómez-Sánchez R, Rose J, Guimarães R, Mari M, Papinski D, Rieter E, Geerts WJ, Hardenberg R, Kraft C, Ungermann C, *et al.* (2018). Atg9 establishes Atg2-dependent contact sites between the endoplasmic reticulum and phagophores. J Cell Biol 217, 2743–2763.

Gowrishankar S, Lyons L, Rafiq NM, Roczniak-Ferguson A, De Camilli P, Ferguson SM (2021). Overlapping roles of JIP3 and JIP4 in promoting axonal transport of lysosomes in human iPSC-derived neurons. Mol Biol Cell 32, 1094–1103.

Gowrishankar S, Wu Y, Ferguson SM (2017). Impaired JIP3-dependent axonal lysosome transport promotes amyloid plaque pathology. J Cell Biol 216, 3291–3305.

Graef M, Friedman JR, Graham C, Babu M, Nunnari J (2013). ER exit sites are physical and functional core autophagosome biogenesis components. Mol Biol Cell 24, 2918–2931.

Guardia CM, Tan XF, Lian T, Rana MS, Zhou W, Christenson ET, Lowry AJ, Faraldo-Gómez JD, Bonifacino JS, Jiang J, *et al.* (2020). Structure of human ATG9A, the only transmembrane protein of the core autophagy machinery. Cell Rep 31, 107837.

Guardia CM, Farías GG, Jia R, Pu J, Bonifacino JS (2016). BORC functions upstream of kinesins 1 and 3 to coordinate regional movement of lysosomes along different microtubule tracks. Cell Rep 17, 1950–1961.

Guo X, Mattera R, Ren X, Chen Y, Retamal C, González A, Bonifacino JS (2013). The adaptor protein-1 μ1B subunit expands the repertoire of basolateral sorting signal recognition in epithelial cells. Dev Cell 27, 353–366.

Hayashi-Nishino M, Fujita N, Noda T, Yamaguchi A, Yoshimori T, Yamamoto A (2009). A subdomain of the endoplasmic reticulum forms a cradle for autophagosome formation. Nat Cell Biol 11, 1433–1437.

Hirst J, Bright NA, Rous B, Robinson MS (1999). Characterization of a fourth adaptor-related protein complex. Mol Biol Cell 10, 2787–2802.

Imai K, Hao F, Fujita N, Tsuji Y, Oe Y, Araki Y, Hamasaki M, Noda T, Yoshimori T (2016). Atg9A trafficking through the recycling endosomes is required for autophagosome formation. J Cell Sci 129, 3781–3791.

Ivankovic D, Drew J, Lesept F, White IJ, López Doménech G, Tooze SA, Kittler JT (2020). Axonal autophagosome maturation defect through failure of ATG9A sorting underpins pathology in AP-4 deficiency syndrome. Autophagy 16, 391–407.

Jia R, Guardia CM, Pu J, Chen Y, Bonifacino JS (2017). BORC coordinates encounter and fusion of lysosomes with autophagosomes. Autophagy 13, 1648–1663.

Jordens I, Fernandez-Borja M, Marsman M, Dusseljee S, Janssen L, Calafat J, Janssen H, Wubbolts R, Neefjes J (2001). The Rab7 effector protein RILP controls lysosomal transport by inducing the recruitment of dynein-dynactin motors. Curr Biol 11, 1680–1685.

Kannan M, Bayam E, Wagner C, Rinaldi B, Kretz PF, Tilly P, Roos M, McGillewie L, Bär S, Minocha S, *et al.* (2017). WD40-repeat 47, a microtubule-associated protein, is essential for brain development and autophagy. Proc Natl Acad Sci USA 114, E9308–E9317.

Keren-Kaplan T, Bonifacino JS (2021). ARL8 relieves SKIP autoinhibition to enable coupling of lysosomes to kinesin-1. Curr Biol 31, 540–554.e5.

Khobrekar NV, Quintremil S, Dantas TJ, Vallee RB (2020). The dynein adaptor RILP controls neuronal autophagosome biogenesis, transport, and clearance. Dev Cell 53, 141–153.e4.

Kimura T, Watanabe H, Iwamatsu A, Kaibuchi K (2005). Tubulin and CRMP-2 complex is transported via Kinesin-1. J Neurochem 93, 1371–1382.

Lupas A, Van Dyke M, Stock J (1991). Predicting coiled coils from protein sequences. Science 252, 1162–1164.

Maeda S, Yamamoto H, Kinch LN, Garza CM, Takahashi S, Otomo C, Grishin NV, Forli S, Mizushima N, Otomo T (2020). Structure, lipid scrambling activity and role in autophagosome formation of ATG9A. Nat Struct Mol Biol 27, 1194–1201.

Maliga Z, Junqueira M, Toyoda Y, Ettinger A, Mora-Bermúdez F, Klemm RW, Vasilj A, Guhr E, Ibarlucea-Benitez I, Poser I, *et al.* (2013). A genomic toolkit to investigate kinesin and myosin motor function in cells. Nat Cell Biol 15, 325–334.

Mari M, Griffith J, Rieter E, Krishnappa L, Klionsky DJ, Reggiori F (2010). An Atg9-containing compartment that functions in the early steps of autophagosome biogenesis. J Cell Biol 190, 1005–1022.

Markus SM, Marzo MG, McKenney RJ (2020). New insights into the mechanism of dynein motor regulation by lissencephaly-1. Elife 9, e59737.

Matoba K, Kotani T, Tsutsumi A, Tsuji T, Mori T, Noshiro D, Sugita Y, Nomura N, Iwata S, Ohsumi Y, *et al.* (2020). Atg9 is a lipid scramblase that mediates autophagosomal membrane expansion. Nat Struct Mol Biol 27, 1185–1193.

Matsuda S, Miura E, Matsuda K, Kakegawa W, Kohda K, Watanabe M, Yuzaki M (2008). Accumulation of AMPA receptors in autophagosomes in neuronal axons lacking adaptor protein AP-4. Neuron 57, 730–745.

Matsushita M, Tanaka S, Nakamura N, Inoue H, Kanazawa H (2004). A novel kinesin-like protein, KIF1Bbeta3 is involved in the movement of lysosomes to the cell periphery in non-neuronal cells. Traffic 5, 140–151.

Mattera R, Arighi CN, Lodge R, Zerial M, Bonifacino JS (2003). Divalent interaction of the GGAs with the Rabaptin-5-Rabex-5 complex. EMBO J 22, 78–88.

Mattera R, Park SY, De Pace R, Guardia CM, Bonifacino JS (2017). AP-4 mediates export of ATG9A from the trans-Golgi network to promote autophagosome formation. Proc Natl Acad Sci USA 114, E10697 LP–E10706.

Mattera R, Williamson CD, Ren X, Bonifacino JS (2020). The FTS-Hook-FHIP (FHF) complex interacts with AP-4 to mediate perinuclear distribution of AP-4 and its cargo ATG9A. Mol Biol Cell 31, 963–979.

Mauvezin C, Neisch AL, Ayala CI, Kim J, Beltrame A, Braden CR, Gardner MK, Hays TS, Neufeld TP (2016). Coordination of autophagosome-lysosome fusion and transport by a Klp98A-Rab14 complex in Drosophila. J Cell Sci 129, 971–982.

Mrakovic A, Kay JG, Furuya W, Brumell JH, Botelho RJ (2012). Rab7 and Arl8 GTPases are necessary for lysosome tubulation in macrophages. Traffic 13, 1667–1679.

Muhammad E, Levitas A, Singh SR, Braiman A, Ofir R, Etzion S, Sheffield VC, Etzion Y, Carrier L, Parvari R (2015). PLEKHM2 mutation leads to abnormal localization of lysosomes, impaired autophagy flux and associates with recessive dilated cardiomyopathy and left ventricular noncompaction. Hum Mol Genet 24, 7227–7240.

Nangaku M, Sato-Yoshitake R, Okada Y, Noda Y, Takemura R, Yamazaki H, Hirokawa N (1994). KIF1B, a novel microtubule plus end-directed monomeric motor protein for transport of mitochondria. Cell 79, 1209–1220.

Nieto-Torres JL, Shanahan S-L, Chassefeyre R, Chaiamarit T, Zaretski S, Landeras-Bueno S, Verhelle A, Encalada SE, Hansen M (2021). LC3B phosphorylation regulates FYCO1 binding and directional transport of autophagosomes. Curr Biol 31, S0960-9822(21)00750-8.

Nishimura T, Tamura N, Kono N, Shimanaka Y, Arai H, Yamamoto H, Mizushima N (2017). Autophagosome formation is initiated at phosphatidylinositol synthase-enriched ER subdomains. EMBO J 36, 1719–1735.

Noda T (2017). Autophagy in the context of the cellular membrane-trafficking system: the enigma of Atg9 vesicles. Biochem Soc Trans 45, 1323–1331.

Noda T, Kim J, Huang WP, Baba M, Tokunaga C, Ohsumi Y, Klionsky DJ (2000). Apg9p/Cvt7p is an integral membrane protein required for transport vesicle formation in the Cvt and autophagy pathways. J Cell Biol 148, 465–480.

Ohashi Y, Munro S (2010). Membrane delivery to the yeast autophagosome from the Golgi-endosomal system. Mol Biol Cell 21, 3998–4008.

Olsvik HL, Lamark T, Takagi K, Larsen KB, Evjen G, Øvervatn A, Mizushima T, Johansen T (2015). FYCO1 contains a c-terminally extended, LC3A/B-preferring LC3-interacting region (LIR) motif required for efficient maturation of autophagosomes during basal autophagy. J Biol Chem 290, 29361–29374.

De Pace R, Skirzewski M, Damme M, Mattera R, Mercurio J, Foster AM, Cuitino L, Jarnik M, Hoffmann V, Morris HD, *et al.* (2018). Altered distribution of ATG9A and accumulation of axonal aggregates in neurons from a mouse model of AP-4 deficiency syndrome. PLoS Genet 14, e1007363.

De Pace R, Britt DJ, Mercurio J, Foster AM, Djavaherian L, Hoffmann V, Abebe D, Bonifacino JS (2020). Synaptic vesicle precursors and lysosomes Are transported by different mechanisms in the axon of mammalian neurons. Cell Rep 31, 107775.

Pankiv S, Alemu EA, Brech A, Bruun J-A, Lamark T, Overvatn A, Bjørkøy G, Johansen T (2010). FYCO1 is a Rab7 effector that binds to LC3 and PI3P to mediate microtubule plus end-directed vesicle transport. J Cell Biol 188, 253–269.

Pernigo S, Chegkazi MS, Yip YY, Treacy C, Glorani G, Hansen K, Politis A, Bui S, Dodding MP, Steiner RA (2018). Structural basis for isoform-specific kinesin-1 recognition of Y-acidic cargo adaptors. Elife 7, e38362.

Pernigo S, Lamprecht A, Steiner RA, Dodding MP (2013). Structural basis for kinesin-1:cargo recognition. Science 340, 356–359.

Popovic D, Dikic I (2014). TBC1D5 and the AP2 complex regulate ATG9 trafficking and initiation of autophagy. EMBO Rep 15, 392–401.

Pu J, Schindler C, Jia R, Jarnik M, Backlund P, Bonifacino JS (2015). BORC, a multisubunit complex that regulates lysosome positioning. Dev Cell 33, 176–188.

Raiborg C, Wenzel EM, Pedersen NM, Olsvik H, Schink KO, Schultz SW, Vietri M, Nisi V, Bucci C, Brech A, *et al.* (2015). Repeated ER-endosome contacts promote endosome translocation and neurite outgrowth. Nature 520, 234–238.

Ravikumar B, Acevedo-Arozena A, Imarisio S, Berger Z, Vacher C, O'Kane CJ, Brown SDM, Rubinsztein DC (2005). Dynein mutations impair autophagic clearance of aggregate-prone proteins. Nat Genet 37, 771–776.

Rocha N, Kuijl C, van der Kant R, Janssen L, Houben D, Janssen H, Zwart W, Neefjes J (2009). Cholesterol sensor ORP1L contacts the ER protein VAP to control Rab7-RILP-p150 Glued and late endosome positioning. J Cell Biol 185, 1209–1225.

Rosa-Ferreira C, Munro S (2011). Arl8 and SKIP act together to link lysosomes to kinesin-1. Dev Cell 21, 1171–1178.

Sanger A, Yip YY, Randall TS, Pernigo S, Steiner RA, Dodding MP (2017). SKIP controls lysosome positioning using a composite kinesin-1 heavy and light chain-binding domain. J Cell Sci 130, 1637–1651.

Santama N, Krijnse-Locker J, Griffiths G, Noda Y, Hirokawa N, Dotti CG (1998). KIF2β, a new kinesin superfamily protein in non-neuronal cells, is associated with lysosomes and may be implicated in their centrifugal translocation. EMBO J 17, 5855 LP–5867.

Schneider CA, Rasband WS, Eliceiri KW (2012). NIH Image to ImageJ: 25 years of image analysis. Nat Methods 9, 671–675.

Schroeder CM, Vale RD (2016). Assembly and activation of dynein-dynactin by the cargo adaptor protein Hook3. J Cell Biol 214, 309–318.

Stavoe AKH, Hill SE, Hall DH, Colón-Ramos DA (2016). KIF1A/UNC-104 transports ATG-9 to regulate neurodevelopment and autophagy at synapses. Dev Cell 38, 171–185.

Suzuki K, Akioka M, Kondo-Kakuta C, Yamamoto H, Ohsumi Y (2013). Fine mapping of autophagy-related proteins during autophagosome formation in Saccharomyces cerevisiae. J Cell Sci 126, 2534–2544.

Tanaka Y, Kanai Y, Okada Y, Nonaka S, Takeda S, Harada A, Hirokawa N (1998). Targeted disruption of mouse conventional kinesin heavy chain, kif5B, results in abnormal perinuclear clustering of mitochondria. Cell 93, 1147–1158.

Verhey KJ, Kaul N, Soppina V (2011). Kinesin assembly and movement in cells. Annu Rev Biophys 40, 267–288.

Verkerk AJ, Schot R, Dumee B, Schellekens K, Swagemakers S, Bertoli-Avella AM, Lequin MH, Dudink J, Govaert P, van Zwol AL, *et al.* (2009). Mutation in the AP4M1 gene provides a model for neuroaxonal injury in cerebral palsy. Am J Hum Genet 85, 40–52.

Wang W, Lundin VF, Millan I, Zeng A, Chen X, Yang J, Allen E, Chen N, Bach G, Hsu A, *et al.* (2012). Nemitin, a novel Map8/Map1s interacting protein with Wd40 repeats. PLoS One 7, e33094.

Watt D, Dixit R, Cavalli V (2015). JIP3 activates kinesin-1 motility to promote axon elongation. J Biol Chem 290, 15512–15525.

Wijdeven RH, Janssen H, Nahidiazar L, Janssen L, Jalink K, Berlin I, Neefjes J (2016). Cholesterol and ORP1L-mediated ER contact sites control autophagosome transport and fusion with the endocytic pathway. Nat Commun 7, 11808.

Willett R, Martina JA, Zewe JP, Wills R, Hammond GRV, Puertollano R (2017). TFEB regulates lysosomal positioning by modulating TMEM55B expression and JIP4 recruitment to lysosomes. Nat Commun 8, 1580.

Xu L, Sowa ME, Chen J, Li X, Gygi SP, Harper JW (2008). An FTS/Hook/p107(FHIP) complex interacts with and promotes endosomal clustering by the homotypic vacuolar protein sorting complex. Mol Biol Cell 19, 5059–5071.

Yamada T, Carson AR, Caniggia I, Umebayashi K, Yoshimori T, Nakabayashi K, Scherer SW (2005). Endothelial nitric-oxide synthase antisense (NOS3AS) gene encodes an autophagy-related protein (APG9-like2) highly expressed in trophoblast. J Biol Chem 280, 18283–18290.

Yamamoto H, Kakuta S, Watanabe TM, Kitamura A, Sekito T, Kondo-Kakuta C, Ichikawa R, Kinjo M, Ohsumi Y (2012). Atg9 vesicles are an important membrane source during early steps of autophagosome formation. J Cell Biol 198, 219–233.

Ylä-Anttila P, Vihinen H, Jokitalo E, Eskelinen E-L (2009). 3D tomography reveals connections between the phagophore and endoplasmic reticulum. Autophagy 5, 1180–1185.

Young ARJ, Chan EYW, Hu XW, Köchl R, Crawshaw SG, High S, Hailey DW, Lippincott-Schwartz J, Tooze SA (2006). Starvation and ULK1-dependent cycling of mammalian Atg9 between the TGN and endosomes. J Cell Sci 119, 3888–3900.

Zavodszky E, Vicinanza M, Rubinsztein DC (2013). Biology and trafficking of ATG9 and ATG16L1, two proteins that regulate autophagosome formation. FEBS Lett 587, 1988–1996.